Monthly Notices of the ROYAL ASTRONOMICAL SOCIETY

MNRAS **544,** 836–854 (2025) https://doi.org/10.1093/mnras/staf1732
Advance Access publication 2025 October 10

Improved late-time fits with wavelet extensions of ΛCDM

Luis A. Escamilla [1,2★] Emre Özülker,[1] Özgür Akarsu [2] Eleonora Di Valentino [1] and J. A. Vázquez [3]

[1]*School of Mathematical and Physical Sciences, University of Sheffield, Hounsfield Road, Sheffield S3 7RH, UK*
[2]*Department of Physics, Istanbul Technical University, Maslak 34469, Istanbul, Türkiye*
[3]*Instituto de Ciencias Físicas, Universidad Nacional Autónoma de México, Cuernavaca, Morelos 62210, México*

Accepted 2025 October 8. Received 2025 October 8; in original form 2025 February 25

ABSTRACT

We parametrize the Hubble function by adding Hermitian wavelets to the Hubble radius of Λ cold dark matter (ΛCDM). This construction enables the Hubble function to oscillate around ΛCDM at late times while preserving the angular diameter distance to the last scattering. We perform parameter inference and model selection at the background level using a wide range of cosmological observations. We find that baryon acoustic oscillation (BAO) data play a central role in constraining the wavelet parameters. In particular, we focus on the differences between SDSS and DESI BAO data sets. Wavelet models consistently provide a better fit when either BAO data set is included. DESI-BAO prefers wavelets centred around $z \sim 0.7$, while SDSS-BAO prefers higher redshifts ($z > 1$), driven by discrepancies in their D_H/r_d measurements at $z = 0.51$ and $z \sim 2.3$. We also analyse the consequences for a dynamical dark energy component derived from the wavelet modifications. The dark energy density is found to oscillate by construction and can become negative at large redshifts ($z \gtrsim 2$) in response to the SDSS-BAO data. Notably, the early Universe constraints, including those on the matter density and Hubble constant, remain essentially unchanged. Our results indicate that wavelet-based deviations are favoured in the late Universe, with DESI-BAO leading to a significant improvement of more than 3σ in the fit. These findings suggest that localized oscillatory features in the expansion history may help reconcile tensions in low-redshift data without disrupting early-Universe consistency.

Key words: methods: statistical – cosmological parameters – cosmology: theory – dark energy – distance scale – large-scale structure of Universe.

1 INTRODUCTION

The standard model of cosmology, the Λ cold dark matter (CDM) model dubbed ΛCDM, provides excellent accuracy in explaining the majority of high-precision cosmological observations despite the simplicity of the model (S. Perlmutter et al. 1998, 1999; A. G. Riess et al. 1998; K. N. Abazajian et al. 2009; R. Amanullah et al. 2010; W. J. Percival et al. 2010; B. A. Reid et al. 2010; E. Komatsu et al. 2011; C. L. Bennett et al. 2013; M. Li et al. 2013; D. H. Weinberg et al. 2013; R. Adam et al. 2016; N. Aghanim et al. 2020; V. Mossa et al. 2020; S. Aiola et al. 2020; S. Alam et al. 2021; L. Balkenhol et al. 2023). Nevertheless, it faces numerous challenges, both theoretical and statistical. The most prominent of these are the Cosmological Constant Problem (S. Weinberg 1989; L.-M. Wang et al. 2000; V. Sahni 2002) and the Coincidence Problem (V. Sahni 2004; U. Alam, V. Sahni & A. A. Starobinsky 2004; P. Bull et al. 2016) on the theoretical side, and the H_0 tension (L. Verde, T. Treu & A. G. Riess 2019; L. Knox & M. Millea 2020; E. Di Valentino et al. 2021b, d; A. G. Riess et al. 2022; M. Kamionkowski & A. G. Riess 2023; Y. S. Murakami et al. 2023; L. Verde, N. Schöneberg & H. Gil-Marín 2024; E. Di Valentino & D. Brout 2024; L. Breuval et al. 2024; S. Li et al. 2024; L. Perivolaropoulos 2024) and the S_8 tension (E. Di Valentino & S. Bridle 2018; M. Douspis, L. Salvati & N. Aghanim 2018; T. Tröster et al. 2020; C. Heymans et al. 2021; E. Di Valentino et al. 2021c; T. M. C. Abbott et al. 2022, 2023; R. Dalal et al. 2023; A. Dvornik et al. 2023; S. A. Adil et al. 2023; S. Chen et al. 2024; J. Kim et al. 2024; L. Faga et al. 2024; J. Harnois-Deraps et al. 2024; Ö. Akarsu et al. 2025c) on the observational side; see also E. Abdalla et al. 2022, L. Perivolaropoulos & F. Skara 2022, E. Di Valentino 2022, O. Akarsu et al. 2024c, and E. Di Valentino et al. 2025 for reviews of the tensions and anomalies in cosmology.

A plethora of alternative models to ΛCDM have been proposed to provide a better description of the observed Universe, such as Interacting DE models (R. Murgia, S. Gariazzo & N. Fornengo 2016; A. Pourtsidou & T. Tram 2016; R. C. Nunes et al. 2016; S. Kumar & R. C. Nunes 2016, 2017; E. Di Valentino, A. Melchiorri & O. Mena 2017; W. Yang et al. 2018, 2020a; E. Di Valentino et al. 2020; M. Lucca & D. C. Hooper 2020; E. Di Valentino & O. Mena 2020; S. Kumar 2021; R. C. Nunes & E. Di Valentino 2021; S. Gariazzo et al. 2022; A. Bernui et al. 2023; K. R. Mishra et al. 2023; G. Liu et al. 2023; S. Pan & W. Yang 2023; Y. Zhai et al. 2023; M. A. van der Westhuizen & A. Abebe 2024; Y.-H. Yao & X.-H. Meng 2023; S. Castello et al. 2024; M. Forconi et al. 2024; G. Garcia-Arroyo, López L. A. Ureña López & J. A. Vázquez 2024; D. Benisty et al. 2024; E. Silva et al. 2024, 2025; W. Giarè et al. 2024; H. Bagherian et al. 2025; G. A. Hoerning et al. 2025; M. A. Sabogal et al. 2025; M. Scherer et al. 2025), extended parameter spaces (E. Di Valentino, A.

★ E-mail: luis.escamilla@icf.unam.mx

Melchiorri & J. Silk 2016), Vacuum phase transition (E. Di Valentino, E. V. Linder & A. Melchiorri 2018b), evolving DE or Late-time solutions (K. Dutta et al. 2020; R. von Marttens et al. 2020; O. Akarsu et al. 2020b; E. Di Valentino, A. Mukherjee & A. A. Sen 2021a; E. Di Valentino 2021; W. Yang et al. 2021b; E. Di Valentino et al. 2022; L. Heisenberg, H. Villarrubia-Rojo & J. Zosso 2023; W. Giarè 2023; A. Lapi et al. 2023; S. A. Adil et al. 2024; A. Gómez-Valent et al. 2024; D. Bousis & L. Perivolaropoulos 2024; X. Tang et al. 2024; J.-Q. Jiang et al. 2024; M. T. Manoharan 2024; A. Krolewski, W. J. Percival & A. Woodfinden 2025; E. Specogna et al. 2025; E. Özülker, E. Di Valentino & W. Giarè 2025; D. H. Lee et al. 2025), Early DE or solutions (V. Poulin et al. 2019, 2021, 2025; T. L. Smith, V. Poulin & M. A. Amin 2020; C. Krishnan et al. 2020; F. Niedermann & M. S. Sloth 2021; N. Schöneberg et al. 2022; G. Ye, J. Zhang & Y.-S. Piao 2023; F. Niedermann & M. S. Sloth 2022, 2023; D. H. F. de Souza & R. Rosenfeld 2023; V. Poulin, T. L. Smith & T. Karwal 2023; J. S. Cruz, F. Niedermann & M. S. Sloth 2023; S. Vagnozzi 2023; J. L. Cervantes-Cota, Galindo-Uribarri & N. Smoot 2023; G. Efstathiou, E. Rosenberg & V. Poulin 2024; M. Garny et al. 2024; W. Giarè 2024; J. Kochappan et al. 2024; W. Giarè et al. 2025; D. Pedrotti et al. 2025), late time or local transitions (E. Di Valentino et al. 2019; G. Alestas et al. 2022; E. Frion et al. 2023; Rathore H. Ruchika et al. 2024; P. L. Ruchika et al. 2025), negative or sign-switching DE (L. Visinelli, S. Vagnozzi & U. Danielsson 2019; O. Akarsu et al. 2020b, 2021, 2023a, 2023c, 2024a; G. Ye & Y.-S. Piao 2020; R. Calderón et al. 2021; A. A. Sen, S. A. Adil & S. Sen 2022; S. Di Gennaro & Y. C. Ong 2022; Y. C. Ong 2023; L. A. Anchordoqui, I. Antoniadis & D. Lust 2024b; S. A. Adil et al. 2024; S. Halder et al. 2024; L. A. Anchordoqui et al. 2024a; Ö. Akarsu et al. 2024d, 2025a, 2025b; A. Yadav et al. 2025; E. A. Paraskevas et al. 2024; A. Gomez-Valent & J. Solà Peracaula 2024; Y. Toda et al. 2024; A. Gómez-Valent & J. Solà Peracaula 2025; M. S. Souza et al. 2025; J. F. Soriano, S. Wohlberg & L. A. Anchordoqui 2025; L. A. Escamilla et al. 2025; M. Bouhmadi-López & B. Ibarra-Uriondo 2025), Emerging DE (S. Pan et al. 2020; W. Yang et al. 2020b, 2021a), DM solutions or neutrinos (E. Di Valentino et al. 2018a; L. A. Anchordoqui et al. 2022; S. Pan et al. 2024; I. J. Allali, D. Aloni & N. Schöneberg 2024; R. T. Co et al. 2024; A. Aboubrahim & P. Nath 2024), modifications at recombination (N. Lee et al. 2023; K. L. Greene & F.-Y. Cyr-Racine 2023; K. Greene & F.-Y. Cyr-Racine 2024; M. Baryakhtar, O. Simon & Z. J. Weiner 2024; O. Seto & Y. Toda 2024; G. P. Lynch, L. Knox & J. Chluba 2024; Y. Toda et al. 2024; N. Schöneberg & L. Vacher 2025), Modified Gravity (A. De Felice, S. Mukohyama & M. C. Pookkillath 2021; M. Högås & E. Mörtsell 2023; Y. Tiwari, B. Ghosh & R. K. Jain 2024; R. Y. Wen et al. 2024; C. Pitrou & J.-P. Uzan 2024; O. Akarsu et al. 2024a,b; S. Dwivedi & M. Högås 2024; G. Montani et al. 2025; M. Högås & E. Mörtsell 2025) and many studies work on reconstructing the expansion history or relevant cosmological functions from the available cosmological data (J. A. Vazquez et al. 2012; E. Aubourg et al. 2015; Y. Wang et al. 2018; V. Poulin et al. 2018; D. Tamayo & J. A. Vazquez 2019; E. O. Colgáin, M. M. Sheikh-Jabbari & L. Yin 2021; A. Bonilla, S. Kumar & R. C. Nunes 2021; I. Gómez-Vargas et al. 2023; L. A. Escamilla & J. A. Vazquez 2023; M. Raveri et al. 2023; L. Pogosian et al. 2022; R. C. Bernardo et al. 2022; L. A. Escamilla et al. 2023; R. Calderon et al. 2024; M. A. Sabogal et al. 2024; P. Mukherjee & A. A. Sen 2025). However, it is still far from clear what it takes for a model to overcome the challenges faced by ΛCDM. Due to the success of the ΛCDM model in accurately explaining most observations, a considerable number of proposed alternatives act as extensions or slight deviations from the standard model. In this way, many of the characteristics that contribute to the success of the standard model are preserved. It has recently been shown by O. Akarsu et al. (2023b) that, due to the very high precision of the measurement of the angular scale of the sound horizon at last scattering from the cosmic microwave background (CMB) observations by the *Planck* collaboration (N. Aghanim et al. 2020), if an alternative model retains the consistency of ΛCDM with this measurement without modifying the comoving size of the sound horizon and the H_0 parameter, the Hubble radius $H^{-1}(z)$ of that alternative model should deviate from ΛCDM in the form of *admissible wavelets*, which are localized oscillatory functions with a vanishing integral.

Wavelets can also be conveniently built by differentiating probability density functions, and they provide an arbitrary number of oscillations through differentiation without increasing the number of free parameters. These deviations from ΛCDM, at the background level, can then be mapped to underlying physics, such as an evolving dark energy (DE) density or time-varying gravitational coupling (O. Akarsu et al. 2023b). In this regard, to gain insight into potential solutions to the inherent problems of the standard model, a wavelet extension of ΛCDM can be characterized using parameter inference techniques such as Markov Chain Monte Carlo (MCMC) or Nested Sampling.

In this paper, we study how a wavelet-extension scenario of the standard model performs compared to ΛCDM when applying parameter-inference and model-selection procedures. The paper is organized as follows: in Section 2, we describe the wavelet deviations in the Hubble radius studied in this paper; in Section 3, we present the data sets and methodology used; in Section 4, we discuss the results; and in Section 5, we conclude with our findings.

2 WAVELET DEVIATIONS IN THE HUBBLE RADIUS

Wavelets are localized oscillatory functions, where 'localized' means that they either have compact support or they approximate compact support by decaying rapidly[1]. In this paper, we will use them to write down Hubble radii, $H^{-1}(z)$, whose deviations from the Hubble radius of the ΛCDM model are wavelets. That is, for a given wavelet $\psi(z)$, we write

$$\frac{1}{H(z)} = \frac{1}{\mathcal{H}(z)} + \psi(z) \tag{1}$$

where $\mathcal{H}(z)$ is the usual Hubble function of the ΛCDM model, which reads

$$3\mathcal{H}^2(z) = \rho_{\mathrm{m},0}(1+z)^3 + \rho_{\mathrm{r},0}(1+z)^4 + \rho_\Lambda, \tag{2}$$

with z being the redshift and ρ_i denoting the energy density of the matter (m), radiation (r), and cosmological constant (Λ) components, using the unit convention $8\pi G = c = 1$. In the following, the index '0' denotes the present value of any quantity. This framework implicitly assumes the Robertson–Walker (RW) metric from which the Hubble functions are defined, and, as usual, the metric associated with the ΛCDM model is spatially flat.

These sorts of deviations from the Hubble radius of ΛCDM, defined by equation (1), were first considered in O. Akarsu et al. 2023b. It was shown that for a given $\mathcal{H}(z)$ in agreement with CMB measurements of the angular scale of the sound horizon at last scattering, any deviation in the Hubble radius that retains this

[1]This behaviour can be observed in Fig. 1, where the deviations from ΛCDM (dashed line) characterized by underlying wavelets are oscillatory and approximately vanish outside of a finite range of redshift.

agreement must be an admissible wavelet[2] unless the value of H_0 and/or the comoving length of the sound horizon is also modified. It is crucial to clarify that, in the present paper, despite making use of the same wavelet framework described by equation (1), we do not require $\mathcal{H}(z)$ itself to agree with CMB measurements; rather, we simply use wavelets on top of $\mathcal{H}(z)^{-1}$ to construct Hubble functions that oscillate around the functional form of ΛCDM due to the ability of wavelets to provide an arbitrary number of oscillations with a limited number of free parameters.

It is useful to relate the parameters of $\mathcal{H}(z)$ and $H(z)$. A conveniently simple relation exists between the deceleration parameters of the Hubble functions, that is,

$$q(z) = \mathcal{Q}(z) + \frac{\mathrm{d}\psi(z)}{\mathrm{d}t}, \tag{3}$$

where $q(z)$ and $\mathcal{Q}(z)$ are the usual deceleration parameters for the metric solutions associated with $H(z)$ and $\mathcal{H}(z)$, respectively. A special case of particular interest is a scenario in which all deviations of $H(z)$ from $\mathcal{H}(z)$ arise due to a dynamical dark energy density, $\rho_{\rm DE}(z)$, which replaces ρ_Λ of the ΛCDM model, namely, the scenario with

$$3H^2(z) = \rho_{\rm m,0}(1+z)^3 + \rho_{\rm r,0}(1+z)^4 + \rho_{\rm DE}(z). \tag{4}$$

Defining the normalized deviation between the Hubble functions,

$$\delta(z) \equiv \frac{H(z) - \mathcal{H}(z)}{\mathcal{H}(z)}, \tag{5}$$

one has

$$\rho_{\rm DE}(z) = \rho_{\rm DE,0} + 3\mathcal{H}^2(z)\delta(z)[2 + \delta(z)]. \tag{6}$$

Moreover, we can obtain a DE equation of state (EoS) parameter as

$$w_{\rm DE}(z) = -1 + \frac{2(1+z)\mathcal{H}^2}{\rho_{\rm DE}}\left(\frac{\mathcal{H}'}{\mathcal{H}}\delta(\delta+2) + \delta'(\delta+1)\right), \tag{7}$$

and from this one can define the DE inertial mass density, $\varrho_{\rm DE} \equiv \rho_{\rm DE}(1 + w_{\rm DE})$, which reads

$$\varrho_{\rm DE}(z) = 2(1+z)\mathcal{H}^2\left(\frac{\mathcal{H}'}{\mathcal{H}}\delta(\delta+2) + \delta'(\delta+1)\right), \tag{8}$$

where the prime denotes differentiation with respect to the redshift (we have dropped the redshift dependence of the functions for better readability).

Notice that, so far, we have not made any assumptions about $\psi(z)$ other than it being a wavelet. A reliable way to obtain wavelets is by differentiating probability density functions. In parallel to O. Akarsu et al. 2023b, for the analyses in this paper, we will consider the family of Hermitian wavelets obtained from the derivatives of the Gaussian distribution-in fact, wavelets obtained from probability density functions generically satisfy the admissibility condition, which was a crucial point in O. Akarsu et al. 2023b, but not here. Let us define a Gaussian distribution

$$G(z) = -\frac{\alpha_h}{2\beta_h}e^{-\beta_h(z-z^\dagger)^2}, \tag{9}$$

where $\beta_h > 0$ and α_h can take any value, with the minus sign in front of the function being our convention (since this function can be negative depending on the sign of α_h, strictly speaking, it is not a probability density function). Then, a family of wavelets can be

[2]Wavelets that satisfy the admissibility condition have a vanishing integral over their whole domain; hence, the angular diameter distance to the last scattering surface is preserved in the deviated scenario.

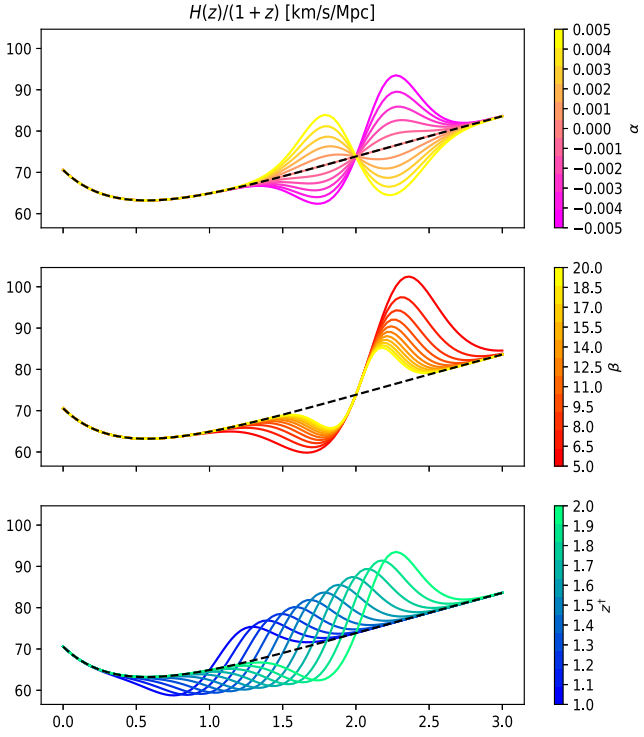

Figure 1. Visual representation of how the underlying Hermitian wavelet (specifically ψ_1) affects the comoving Hubble parameter $H(z)/(1+z)$, where $H(z) = \frac{H_{\Lambda\rm CDM}(z)}{1+\psi(z)H_{\Lambda\rm CDM}(z)}$, when varying each parameter individually. The upper plot corresponds to the parameter α_h in the interval $[-0.005, 0.005]$, the middle one to $\beta_h = [5, 20]$, and the lower one to $z^\dagger = [1.0, 2.0]$. The black dashed line represents $H_{\Lambda\rm CDM}(z)/(1+z)$.

defined where the nth member of the family corresponds to the $n^{\rm th}$ derivative of $G(z)$ for $n > 0$, i.e.

$$\psi_n(z) \equiv \frac{\mathrm{d}^n G(z)}{\mathrm{d}z^n}, \tag{10}$$

yielding

$$\psi_1(z) = -2\beta_h\left[z - z^\dagger\right]G(z), \tag{11a}$$

$$\psi_2(z) = 4\beta_h\left[\beta_h(z-z^\dagger)^2 - \tfrac{1}{2}\right]G(z), \tag{11b}$$

$$\psi_3(z) = -8\beta_h^2\left[\beta_h(z-z^\dagger)^3 - \tfrac{3}{2}(z-z^\dagger)\right]G(z), \tag{11c}$$

$$\psi_4(z) = 16\beta_h^2\left[\beta_h^2(z-z^\dagger)^4 - 3\beta_h(z-z^\dagger)^2 + \tfrac{3}{4}\right]G(z), \tag{11d}$$

and so on. This method of generating wavelets has the convenience of allowing one to control the number of nodes (crossings of zero) of the wavelet, hence the number of oscillations. Although $G(z)$ can be considered the zeroth-order wavelet, it has no nodes and does not oscillate. In comparison, every differentiation introduces one node to the wavelet, e.g. ψ_1 has a single node corresponding to one bump and one dip in the functional form; see Fig. 1. In the following sections, we make use of the first four Hermitian wavelets given in equation (11) to conduct our observational analyses.

3 DATA SETS AND METHODOLOGY

To compare the standard model against our wavelet-extension, we will utilize the Bayesian framework in the form of a parameter inference procedure, which requires the use of data and a sampler code.

Our data sets consist of various combinations of observations related to the cosmic microwave background (CMB), baryon acoustic oscillations (BAO), type Ia supernovae (SN Ia) light curves, cosmic chronometers, and SN Ia absolute magnitudes. Specifically, the following data related to the above observations are used. We used the collection of 31 cosmic chronometers (R. Jimenez et al. 2003; J. Simon, L. Verde & R. Jimenez 2005; D. Stern et al. 2010; M. Moresco et al. 2012, 2016; C. Zhang et al. 2014; M. Moresco 2015), found within the repository (M. Moresco 2015), in combination with the catalogue of the Pantheon + SN Ia sample, covering a redshift range of $0.001 < z < 2.26$ with 1701 light curves of 1550 distinguishable SN Ia (D. M. Scolnic et al. 2018). The associated complete covariance matrix is composed of a statistical part and a systematic part, which, together with the data, is provided in the repository (PantheonPlusSH0ES 2022). These two data sets will always be used together and will be jointly referred to as **SN**. We employ two different BAO data sets. The first data set contains SDSS, BOSS, and eBOSS surveys (S. Alam et al. 2021), in which the Lyman α forest BAO measurements that cover a redshift up to $z \approx 2.34$ are also included. This data set will be referred to as **SB**, which stands for 'SDSS-BAO'. The other data set consists of BAO distance measurements from the first year of the Dark Energy Spectroscopic Instrument (DESI; A. G. Adame et al. 2025), hereafter referred to as **DB** (for DESI-BAO); this data set also includes Lyman α measurements. To avoid double-counting, these measurements will not be combined with their **SB** counterparts; rather, we investigate in the next section the consequences of using two different BAO data sets. In some instances, we will also use a Gaussian prior of $H_0 = 73.04 \pm 1.04\,\mathrm{km\,s^{-1}\,Mpc^{-1}}$ from the local distance ladder measurements of the SH0ES team, based on the calibration of the absolute magnitude of SN Ia with Cepheid variables (A. G. Riess et al. 2022). When this prior is in use, we denote it by adding **H0** in the name of the combination of data sets. Finally, we will also make use of some background information from the Cosmic Microwave Background (CMB) from the Planck satellite in the form of a 'BAO data point' at a redshift of $z \sim 1100$. The background-level information of the CMB can be encapsulated by the three parameters (E. Aubourg et al. 2015): ω_b (physical baryon density parameter), ω_m (physical matter density parameter), and $D_\mathrm{M}(\sim 1100)/r_\mathrm{d}$, where r_d is the comoving size of the sound horizon at the drag epoch and $D_\mathrm{M}(z)$ is the comoving angular diameter distance to z. This data set will be referred to as **Pl**.

To calculate χ^2 for each data sample, we have

$$\chi^2_\mathrm{data} = (d_{i,m} - d_{i,\mathrm{obs}})^T C^{-1}_{ij,\mathrm{data}} (d_{j,m} - d_{j,\mathrm{obs}}), \tag{12}$$

where d_m and d_obs are our model predictions and the observables, respectively, and C_data is the covariance matrix associated with each of the data sets. Since observations of each data set are independent of each other, the joint χ^2 can be computed as

$$\chi^2_\mathrm{total} = \chi^2_\mathrm{Pl} + \chi^2_\mathrm{SN} + \chi^2_\mathrm{BAO} + \chi^2_\mathrm{H0}, \tag{13}$$

where some terms may not be present depending on the data set combination used, and the index of BAO will refer to either **SB** or **DB**.

For the determination of the optimal parameter values of our model, we employ an adapted version of a Monte Carlo Markov Chain (MCMC) code known as SimpleMC (see A. Slosar & J. A. Vazquez 2019). SimpleMC is designed to calculate expansion rates and distances based on a given Friedmann equation, allowing for the analysis of the data at the background level. More information on the application of this code can be found in the Bayesian inference review presented in (L. E. Padilla et al. 2021). Additionally, our implementation uses `dynesty`, a nested sampling library described in J. S. Speagle 2020, to efficiently compute the Bayesian evidence $E(D|M)$, where D is the data used and M is the sampled model. This evidence can be used to compare two distinct models by using the following relationship:

$$B_{12} \equiv \frac{E(D|M_1)}{E(D|M_2)}, \tag{14}$$

where B_{12} is known as the *Bayes Factor*, with M_1 and M_2 being the two models to be compared. By taking the natural logarithm of this quotient, together with the Jeffreys' scale shown in Table 1 (R. Trotta 2008; B. Efron et al. 2001; R. E. Kass & A. E. Raftery 1995), a useful empirical tool for performing model selection arises. That is, we can use it to gain insight into how well model M_1 compares to model M_2.

Table 1. Jeffreys' scale for model selection based on the logarithm of the Bayes' factor. A positive value of $\ln B_{12}$ indicates evidence in favour of M_1, while a negative value indicates evidence in favour of M_2, following the convention from (R. Trotta 2008).

$\ln B_{12}$	Odds	Probability	Strength of evidence
< 1.0	$< 3{:}1$	< 0.75	Inconclusive
1.0	$\sim 3{:}1$	0.750	Weak evidence
2.5	$\sim 12{:}1$	0.923	Moderate evidence
5.0	$\sim 150{:}1$	0.993	Strong evidence

To make our statistical analysis more robust we also make use of the Bayesian suspiciousness (W. Handley & P. Lemos 2019). This quantity is designed to disentangle the contribution of prior volume effects from the assessment of data set concordance. Given two data sets D_1 and D_2 and a model M, the Bayes ratio is defined as

$$R \equiv \frac{Z_{12}}{Z_1 Z_2}, \tag{15}$$

where Z_{12} is the Bayesian evidence for the combined data sets and Z_i are the evidences for the individual data sets. The Bayes ratio R contains both statistical (likelihood-driven) and prior-volume effects. Suspiciousness isolates the purely statistical contribution by correcting for the information gain (measured by the Kullback–Leibler divergence D):

$$\ln S \equiv \ln R - D. \tag{16}$$

Here $D = D_1 + D_2 - D_{12}$, with D_i being the Kullback–Leibler divergence between prior and posterior for each data set, and D_{12} the KL divergence of their combination. This construction generalizes naturally to N data sets:

$$\ln S \equiv \left(\ln Z_{1\cdots N} - \sum_{i=1}^{N} \ln Z_i \right) - \left(\sum_{i=1}^{N} D_i - D_{1\cdots N} \right), \tag{17}$$

where $Z_{1\cdots N}$ and $D_{1\cdots N}$ denote the evidence and KL divergence of the joint analysis. A value of $\ln S$ close to zero indicates that the data sets are statistically consistent under the model, while large negative values correspond to increasing tension. Positive values can be taken as a sign of a great concordance and consistency between data sets under the model.

This combination of tools enables us to perform parameter estimation and model comparison. Regarding the flat priors used for the parameters of the model: $\Omega_\mathrm{m} = [0.1, 0.5]$ for the matter density parameter, $\Omega_\mathrm{b}h^2 = [0.02, 0.025]$ for the physical baryon density, and $h = [0.4, 0.9]$ for the dimensionless reduced Hubble constant (where $h = H_0/100\,\mathrm{km\,s^{-1}\,Mpc^{-1}}$). For the Hermitian wavelets, we need to

Table 2. Flat prior ranges for the parameters of the Hermitian wavelets used in the analysis.

Models	Priors
$\psi_1, \psi_2, \psi_3, \psi_4$	$\beta_h : [0.01, 25.0]$
$\psi_1, \psi_2, \psi_3, \psi_4$	$z^\dagger : [0.0, 5.0]$
ψ_1	$\alpha_h : [-0.01, 0.01]$
ψ_2	$\alpha_h : [-0.001, 0.001]$
ψ_3	$\alpha_h : [-0.0001, 0.0001]$
ψ_4	$\alpha_h : [-0.00001, 0.00001]$

be more careful with the selection of our priors, and our selection requires some explanation.

As seen in equation (11), each Hermitian wavelet has three free parameters: α_h, β_h, and $z^\dagger$. Each parameter governs a distinct behaviour of the wavelet: the parameter α_h controls the amplitude; the parameter β_h controls both the 'width' and the amplitude; and $z^\dagger$ determines the centre of the wavelet. For visual reference, in Fig. 1, we show the influence of each parameter on $H(z)/(1+z)$. An important thing to note is that the sensitivity of the amplitude of wavelets with respect to the parameter α_h increases with higher-order wavelets. Thus, its prior range decreases by an order of magnitude when moving from ψ_i to ψ_{i+1}. Therefore, our priors for each parameter are $\beta_h : [0.01, 25.0]$ and $z^\dagger : [0.0, 5.0]$ for every wavelet; meanwhile, we set $\alpha_h : [-0.01, 0.01]$ for ψ_1, $\alpha_h : [-0.001, 0.001]$ for ψ_2, $\alpha_h : [-0.0001, 0.0001]$ for ψ_3 and $\alpha_h : [-0.00001, 0.00001]$ for ψ_4 (for reference, they can be found in Table 2).

4 RESULTS

In this section, we present the results of our sampling process, with a particular focus on the differences between the two BAO data sets. Due to the high number of data set combinations used, we visualize only a selection of the plots and comment on others as necessary. For completeness, the best-fitting values of h and $\Omega_{\mathrm{m},0}$, as well as the Bayes' factors and $-2\Delta \ln \mathcal{L}_{\max}$, for all analyses are provided in Tables 4 and 3.

In Fig. 2, we plot the 1D marginalized posterior distributions of $z^\dagger$ for the first-order wavelet ψ_1. Although we show only one wavelet, similar features are observed in the others (see Appendix A and Fig. A1). A notable feature is the absence of a clear peak in the posterior distribution without BAO data, as seen in the leftmost panel. This situation changes in the middle panel with the inclusion of **SB**, where a distinct peak around $z^\dagger \sim 2.5$ appears when **Pl** is not included (red and green plots). When **Pl** is also included, a bimodal distribution is observed, with a smaller peak around $z^\dagger \sim 1$ and a larger accumulation of probability for $z^\dagger \gtrsim 3$. It is important to note that **Pl** is the only data set used beyond the redshift of 2.34, and the impact of a wavelet at high redshifts does not lead to significant differences when compared with any combination of BAO, **SN**, or **H0** data. Moreover, even though **Pl** is not affected by a high-redshift wavelet as we only do a background analysis for which admissible wavelets induce no changes over ΛCDM when CMB data are considered (see O. Akarsu et al. 2023b). In fact, a high-redshift wavelet well-approximates ΛCDM where data are present; this can be seen by comparing, say, the rightmost panel of Fig. 3 with Fig. 1, where the shape of the ΛCDM curve can be seen in dashed lines. Since the **Pl** data is also not sensitive to high-redshift wavelets, we interpret the change in the posterior of $z^\dagger$ to be due to the restrictions imposed by **Pl** on the baseline ΛCDM parameters (Ω_{m}, h, and $\Omega_{\mathrm{b}}h^2$), which in turn cannot be combined with a wavelet at low redshifts in the presence of low-redshift data. This restriction on baseline parameters becomes evident by comparing the third and fourth panels of Fig. 3, where the ΛCDM-like curves become denser resulting in the removal of some freedom in the expansion history. Finally, we note that the inclusion of **H0** in the data set has almost no impact on the constraints on $z^\dagger$ with or without **SB**.

Moving on to the last panel of Fig. 2, we see that when **DB** is included instead of **SB**, the results are more stable with respect to the addition of **Pl** and the bimodal distribution is present for all data set combinations. More interestingly, the peak at low redshifts moves to around $z^\dagger \sim 0.7$ and the inclusion of the **SN** data strengthens this peak, significantly decreasing the probability around a ΛCDM-like cosmology within the redshift range where data are present. This result is in line with the findings of the DESI collaboration in A. G. Adame et al. 2025 which note a $\sim 2.6\sigma$ preference for dynamical DE (when the DE is allowed to evolve with the Chevallier–Polarski–Linder parametrization) when DESI-BAO is combined with CMB data, which increases to $\sim 3.9\sigma$ when SN Ia data are also included. However, note that they still find only $\sim 2.5\sigma$ evidence when their chosen SN Ia data set is Pantheon+ [(compared to Union3; D. Rubin et al. 2023) or DESY5 (T. M. C. Abbott et al. 2024)], whereas here we find that the preference for a dynamical DE[3] is strengthened with the inclusion of **SN** that consists of Pantheon+ and cosmic chronometers. And, as before, the constraints on $z^\dagger$ are not very sensitive to the inclusion of **H0**.

Regarding the constraints on the parameters α_h and β_h, we consider these results to be less relevant (especially compared to $z^\dagger$) for inclusion in the main text. However, their 1D posteriors and a brief discussion can be found in Appendix A.

In Fig. 3 (see also Fig. A4), we show the Hubble functions corresponding to ψ_1 for BAO + **SN** data set combinations with and without **Pl**, and using both **SB** and **DB**. Similarly to the 1D posterior plots for $z^\dagger$, we limit this discussion to ψ_1 since the behaviours are similar across all wavelets, as shown in Fig. A5. Again, we see the lower-redshift dynamics preferred by **DB** with $z^\dagger \sim 0.7$ compared to the preference for higher $z^\dagger$ values by **SB**. The inclusion of **Pl** causes the ΛCDM parameters to be strictly constrained, and when **SB** is present, in contrast to the **DB** case, it also pushes the wavelets to redshifts mostly irrelevant to our low-redshift data sets. We see that the presence of the wavelets allows for a better fit to the BAO data as argued in O. Akarsu et al. 2023b. However, the $D_H(z)/r_{\mathrm{d}}$ values from the BAO data are also accompanied by $D_{\mathrm{M}}(z)/r_{\mathrm{d}}$ values (also $D_V(z)/r_{\mathrm{d}}$, but we do not discuss them)[4]. In Fig. 4, we also plot the inverted and scaled function $D_{\mathrm{M}}(z)$ for ψ_1 for the combination of data sets selected in the second panel of Fig. 3. It is clear from Figs 3 and 4 that even for this case, where the oscillatory features of the wavelets are readily apparent in the $H(z)/(1+z)$ plots, the $D_{\mathrm{M}}(z)$ function is barely affected by the wavelets. This is due to the $D_{\mathrm{M}}(z)$ function being an integral of the Hubble radius which smooths out the wavelet deviations. Thus, we can safely argue that it is the $D_H(z)/r_{\mathrm{d}}$ measurements from the BAO data that drive the preference for wavelets and not the $D_{\mathrm{M}}(z)/r_{\mathrm{d}}$ measurements. In particular, Fig. 3 indicates that it is the Lyman α $D_H(z)/r_{\mathrm{d}}$ measurement for **SB**, and the $D_H(z)/r_{\mathrm{d}}$ measurement at $z = 0.51$ for **DB** with the 'anomalous' $D_{\mathrm{M}}(z)/r_{\mathrm{d}}$ measurement of **DB** having little to no effect on driving the wavelets.

[3]If the wavelets are assumed to originate from a dynamical DE component as described by equation (6)

[4]For reference, we note that $D_H(z) = c/H(z)$, $D_{\mathrm{M}}(z) = c\int_0^z \mathrm{d}z'/H(z')$ for a spatially flat RW metric, and $D_V(z) = [zD_{\mathrm{M}}(z)^2 D_H(z)]^{1/3}$.

Table 3. First half of the mean values and standard deviations for two of the parameters used in the reconstruction, $\Omega_{m,0}$ and h. For each model, the last two columns present the natural logarithm of the Bayes Factor, $\ln B_{\Lambda\mathrm{CDM},i}$, and $-2\Delta \ln \mathcal{L}_{\max}$, defined as $-2\ln(\mathcal{L}_{\max,i}/\mathcal{L}_{\max,\Lambda\mathrm{CDM}})$, for a comparison of the fit of the data. When BAO data is included, it is denoted as **SB** (SDSS-BAO) in this table.

Model	Data Sets	h	$\Omega_{m,0}$	$\ln B_{\Lambda\mathrm{CDM},i}$	$-2\Delta \ln \mathcal{L}_{\max}$	$\ln S$
ΛCDM	**SB + Pl**	0.679 (0.006)	0.309 (0.007)	0	0	1.25
ψ_1		0.688 (0.006)	0.301 (0.007)	−0.69 (0.34)	−5.08	1.75
ψ_2		0.688 (0.006)	0.302 (0.008)	−1.02 (0.35)	−4.94	1.61
ψ_3		0.689 (0.006)	0.301 (0.007)	−0.89 (0.35)	−4.54	1.88
ψ_4		0.689 (0.006)	0.301 (0.008)	−0.75 (0.34)	−4.81	2.01
ΛCDM	**SB + SN**	0.686 (0.013)	0.306 (0.013)	0	0	1.77
ψ_1		0.692 (0.014)	0.315 (0.015)	−0.61 (0.17)	−7.42	2.31
ψ_2		0.692 (0.014)	0.318 (0.016)	−1.22 (0.17)	−8.59	2.59
ψ_3		0.693 (0.014)	0.315 (0.015)	−0.83 (0.18)	−8.07	2.61
ψ_4		0.692 (0.014)	0.314 (0.014)	−0.71 (0.18)	−8.61	2.82
ΛCDM	**SB + SN + Pl**	0.676 (0.006)	0.312 (0.007)	0	0	1.54
ψ_1		0.684 (0.005)	0.306 (0.007)	−0.22 (0.35)	−5.22	1.19
ψ_2		0.685 (0.005)	0.306 (0.006)	−0.51 (0.34)	−4.72	1.11
ψ_3		0.684 (0.005)	0.307 (0.007)	−0.54 (0.34)	−5.29	1.29
ψ_4		0.685 (0.006)	0.306 (0.007)	−0.66 (0.34)	−6.58	1.59
ΛCDM	**SB + SN + H0**	0.709 (0.014)	0.311 (0.013)	0	0	1.88
ψ_1		0.705 (0.012)	0.315 (0.015)	0.14 (0.24)	−2.91	−0.45
ψ_2		0.706 (0.012)	0.318 (0.015)	0.34 (0.24)	−3.17	0.01
ψ_3		0.705 (0.012)	0.314 (0.015)	0.55 (0.23)	−3.89	−0.02
ψ_4		0.705 (0.011)	0.314 (0.015)	−0.11 (0.23)	−3.23	0.04
ΛCDM	**SB + SN + Pl + H0**	0.679 (0.005)	0.308 (0.007)	0	0	0.33
ψ_1		0.687 (0.005)	0.303 (0.007)	−1.38 (0.34)	−6.18	0.57
ψ_2		0.688 (0.005)	0.302 (0.007)	−1.52 (0.34)	−6.34	0.42
ψ_3		0.688 (0.006)	0.302 (0.007)	−1.48 (0.35)	−7.16	0.98
ψ_4		0.688 (0.005)	0.302 (0.006)	−1.21 (0.34)	−7.78	1.08
ΛCDM	**SN + Pl**	0.671 (0.006)	0.319 (0.008)	0	0	0.89
ψ_1		0.681 (0.006)	0.311 (0.008)	−0.02 (0.34)	−2.82	0.43
ψ_2		0.681 (0.006)	0.309 (0.008)	0.22 (0.35)	−3.53	0.41
ψ_3		0.681 (0.006)	0.310 (0.008)	0.52 (0.34)	−3.54	0.49
ψ_4		0.681 (0.006)	0.310 (0.008)	0.28 (0.35)	−4.42	0.51
ΛCDM	**SN + Pl + H0**	0.675 (0.006)	0.314 (0.008)	0	0	−1.05
ψ_1		0.685 (0.006)	0.306 (0.007)	−0.61 (0.34)	−5.56	−0.93
ψ_2		0.685 (0.006)	0.306 (0.007)	−0.69 (0.35)	−6.51	−0.83
ψ_3		0.685 (0.006)	0.306 (0.008)	−0.82 (0.35)	−6.27	−0.61
ψ_4		0.684 (0.006)	0.306 (0.007)	−0.85 (0.35)	−6.37	−0.52

As shown in Tables 4 and 3, while the early Universe constraints on the matter density and the Hubble constant remain unchanged, every case with wavelets provides a better fit to the data, as indicated by the negative $-2\Delta \ln \mathcal{L}_{\max}$ values. This improvement exceeds the expected -3 difference due to the additional three free parameters associated with the wavelets compared to ΛCDM. Notably, when using **DB**, wavelets are favoured at over 3σ[5] in all cases except one (ψ_1 with **DB + Pl**, as seen in Table 4), even with the Planck likelihood[6]. This advantage diminishes when **SB** is used as the BAO data set. This is impressive as the Planck likelihood imposes heavy restrictions on both $\Omega_{m,0}$ and h (as seen in their inferred values and 1σ when the **Pl** data set is present and in Fig. 3 when **Pl** is used) and this in turn could act against our wavelet extension of the standard model. A clear way to verify this is by analysing Fig. 2. When the Planck likelihood is present, we observe a rise in apparent bimodality centred in $z^\dagger \sim 4$. Given the fact that our data span a redshift up to 2.34, if the wavelet is centred way beyond this point (which in this case means centred in $z > 3$), we can assume that the data sets used for the parameter inference stand against the inclusion of the wavelet in the redshift interval covered by them. This is especially true when SDSS-BAO is included, although not with DESI-BAO, which can be verified by referring back to Fig. 3 and the $\Delta \ln \mathcal{L}_{\max}$ values in Tables 4 and 3. These figures (also Figs 4–6) are commonly referred to as *functional posteriors*, i.e. probability distributions over functions implied by a Bayesian posterior on model parameters. Given an MCMC (or nested sampling in our case) chain, each sample of parameters can be mapped to a predicted function (for example, the expansion rate $H(z)$ in cosmology). The PYTHON library `fgivenx` (W. Handley 2018) evaluates these function samples on a grid in x, and compresses them into contour plots representing confidence regions for the functional posterior. In practice, this corresponds to computing the probability density of $f(x)$ at each x and visualizing shaded bands for regions such as 68 per cent and 95 per cent confidence intervals, thereby providing an intuitive summary of parameter uncertainty in function space rather than solely in parameter space. By looking at these functional posteriors, it is clear that, when using **SB** (**DB**), the centre of the wavelet is localized in $z \sim 2.3$ ($z \sim 0.7$), and by adding **Pl**, we observe that the wavelet behaviour is fully displaced with ΛCDM-like behaviour and unconstrained when **SB** is present.

[5]The σ values reported here differ slightly from those reported by the DESI collaboration. Our σ values are obtained via $\sqrt{\Delta\chi^2}$ (i.e. $\sqrt{-2\,\Delta \ln \mathcal{L}}$) and serve as a goodness-of-fit proxy for how strongly a given data set favours a model.

[6]This is again in line with the findings of the DESI collaboration as explained in the previous paragraph of the main text.

Table 4. Second half of the mean values and standard deviations for two of the parameters used in the reconstruction, $\Omega_{m,0}$ and h. In this table, when BAO data are included, it is denoted as **DB** (DESI-BAO). For each model, the last two columns present the natural logarithm of the Bayes Factor, $\ln B_{\Lambda\mathrm{CDM},i}$, and $-2\Delta \ln \mathcal{L}_{\max}$, defined as $-2\ln(\mathcal{L}_{\max,i}/\mathcal{L}_{\max,\Lambda\mathrm{CDM}})$, for a comparison of the fit of the data.

Model	data sets	h	$\Omega_{m,0}$	$\ln B_{\Lambda\mathrm{CDM},i}$	$-2\Delta \ln \mathcal{L}_{\max}$	$\ln S$
ΛCDM	**DB + Pl**	0.677 (0.006)	0.311 (0.008)	0	0	1.01
ψ_1		0.686 (0.008)	0.304 (0.009)	−0.82 (0.34)	−8.18	1.51
ψ_2		0.686 (0.006)	0.303 (0.008)	−0.78 (0.33)	−10.12	0.96
ψ_3		0.687 (0.006)	0.303 (0.007)	−0.84 (0.32)	−10.24	1.21
ψ_4		0.688 (0.006)	0.302 (0.007)	−0.81 (0.34)	−10.48	1.51
ΛCDM	**DB + SN**	0.683 (0.017)	0.313 (0.012)	0	0	2.15
ψ_1		0.679 (0.014)	0.309 (0.012)	−0.12 (0.23)	−11.42	2.01
ψ_2		0.681 (0.013)	0.308 (0.012)	−0.21 (0.23)	−11.08	1.56
ψ_3		0.679 (0.014)	0.308 (0.012)	0.05 (0.24)	−10.92	2.35
ψ_4		0.679 (0.013)	0.309 (0.012)	0.02 (0.22)	−11.22	2.34
ΛCDM	**DB + SN + Pl**	0.675 (0.005)	0.314 (0.007)	0	0	2.35
ψ_1		0.683 (0.005)	0.308 (0.007)	0.01 (0.32)	−11.61	2.98
ψ_2		0.683 (0.005)	0.307 (0.007)	0.05 (0.33)	−10.11	2.13
ψ_3		0.683 (0.006)	0.307 (0.007)	−0.21 (0.32)	−10.65	2.81
ψ_4		0.683 (0.005)	0.308 (0.007)	0.15 (0.31)	−10.25	2.23
ΛCDM	**DB + SN + H0**	0.702 (0.014)	0.311 (0.012)	0	0	0.35
ψ_1		0.703 (0.013)	0.311 (0.011)	−0.14 (0.27)	−11.33	1.54
ψ_2		0.704 (0.013)	0.312 (0.011)	−0.31 (0.23)	−10.86	0.61
ψ_3		0.703 (0.013)	0.311 (0.011)	−0.67 (0.26)	−10.14	1.45
ψ_4		0.704 (0.013)	0.311 (0.012)	−0.56 (0.25)	−10.81	1.56
ΛCDM	**DB + SN + Pl + H0**	0.678 (0.005)	0.311 (0.007)	0	0	0.07
ψ_1		0.686 (0.005)	0.304 (0.007)	−1.61 (0.35)	−13.25	1.85
ψ_2		0.686 (0.005)	0.304 (0.007)	−1.41 (0.34)	−11.87	0.98
ψ_3		0.686 (0.005)	0.304 (0.006)	−1.99 (0.34)	−12.48	1.83
ψ_4		0.686 (0.005)	0.304 (0.007)	−1.31 (0.34)	−12.01	1.88
ΛCDM	**SN**	0.674 (0.027)	0.331 (0.017)	0	0	1.62
ψ_1		0.676 (0.026)	0.331 (0.017)	0.58 (0.23)	−3.71	1.46
ψ_2		0.675 (0.026)	0.332 (0.018)	0.12 (0.24)	−3.85	1.42
ψ_3		0.676 (0.028)	0.332 (0.018)	0.13 (0.22)	−5.21	1.55
ψ_4		0.676 (0.026)	0.330 (0.017)	0.42 (0.23)	−5.41	1.54
ΛCDM	**SN + H0**	0.711 (0.019)	0.322 (0.017)	0	0	0.02
ψ_1		0.711 (0.017)	0.323 (0.016)	−0.28 (0.22)	−3.88	−0.15
ψ_2		0.712 (0.017)	0.323 (0.017)	−0.12 (0.22)	−4.18	−0.12
ψ_3		0.712 (0.017)	0.324 (0.016)	−0.69 (0.22)	−5.04	0.35
ψ_4		0.712 (0.018)	0.322 (0.017)	−0.09 (0.24)	−5.66	0.16

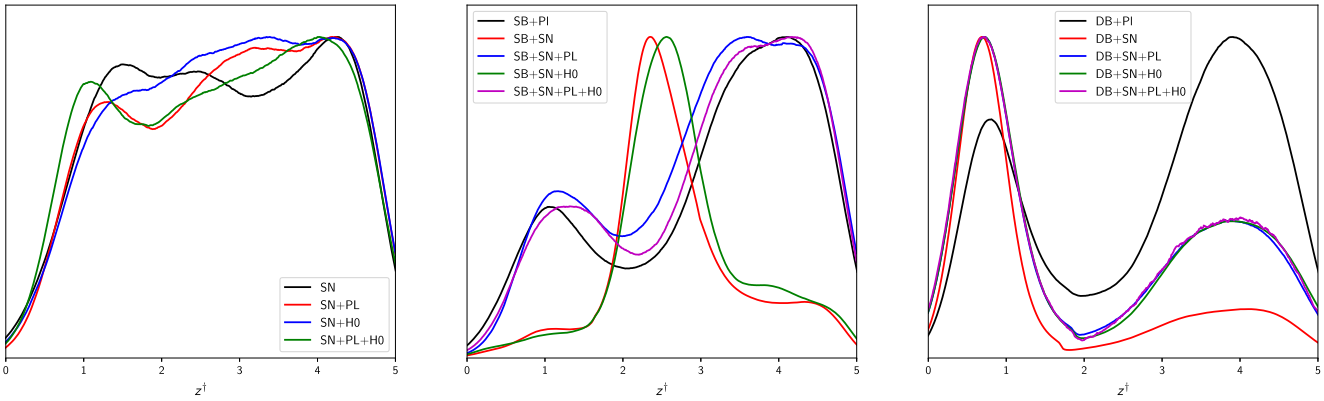

Figure 2. 1D marginalized posterior distributions for the reconstructed parameter $z^\dagger$ for $\psi_1(z)$. We present the results in three different panels to show the effect of BAO data sets on the posteriors: **SB** (SDSS BAO) in the middle panel, **DB** (DESI BAO) in the right panel, and no BAO in the left panel. These plots were made using the PYTHON library GETDIST (A. Lewis 2025).

Focusing now on the Bayesian evidence through the Bayes' factor $\ln B_{\Lambda\mathrm{CDM},i}$ in Tables 4 and 3, we can see some interesting results. Almost every case is as good ($|\ln B| < 1$) or slightly better (with weak evidence in favour of the wavelets according to Jeffreys' scale) than the standard model at explaining the data. The best cases obtained are **DB + SN + Pl + H0** and **SB + SN + Pl + H0**, the reason being that a wavelet-like behaviour seems to be a good alternative to ΛCDM in reconciling the localized dynamical behaviour preferred

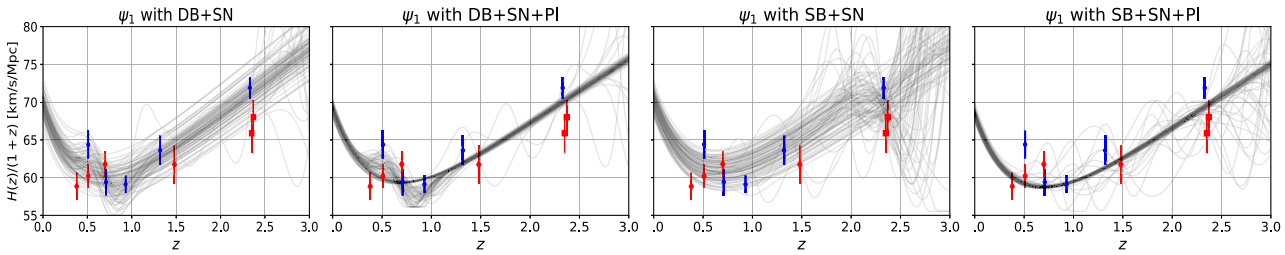

Figure 3. Functional posterior for $H(z)/(1+z)$ for $\psi_1(z)$ using four distinct data combinations: **DB + SN**, **DB + SN + PI**, **SB + SN**, and **SB + SN + PI**. The red (blue) error bars correspond to the SDSS (DESI) BAO distance $D_H(z)/r_d$ measurements. The size of the sound horizon was fixed to the robust value of 147 Mpc to show the BAO data in the figure. The plots were made using the PYTHON library `fgivenx` (W. Handley 2018).

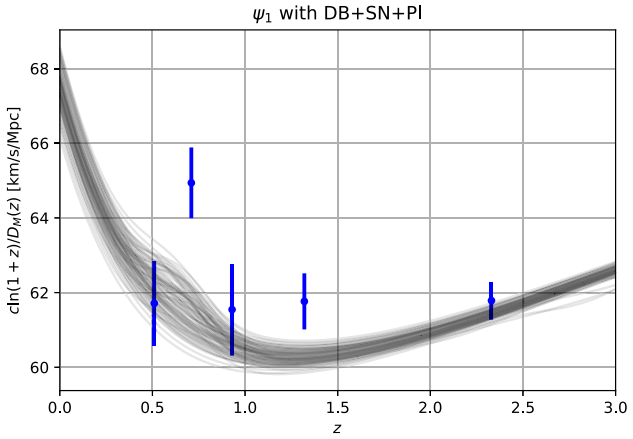

Figure 4. Functional posterior of the inverted and scaled comoving angular diameter distance, $c\ln(1+z)/D_M(z)$, where $D_M(z) = c\int_0^z dz'/H(z')$; note that this function approaches H_0 with $z \to 0$. The blue error bars correspond to the re-scaled D_M measurements from DESI. The functional posterior was made with the reconstructed wavelet ψ_1 using the data set combination **DB + SN + PI**. The size of the sound horizon was fixed to the robust value of 147 Mpc to show the BAO data in the figure. The plot was made using the PYTHON library `fgivenx` (W. Handley 2018).

by both different BAO data sets while preserving the good fit of ΛCDM to the measurements of the first peak of the CMB power spectrum. It is important to stress that the evidence is weak, at best, in favour of the wavelets and it should not be taken as a decisive factor if one wishes to put into question the validity of the standard model.

Let us now see the results pertaining to the Bayesian suspiciousness $\ln S$, as reported in Tables 4 and 3. For combinations without the **H0**, the Hermitian wavelets consistently yield higher $\ln S$ values than ΛCDM, indicating improved concordance between BAO, SN, CC, and CMB data. When SH0ES is included, ΛCDM displays regular concordance (e.g. $\ln S \simeq 0$ for **DB + SN + PI + H0** and **SN + H0**). In these cases, the wavelets increase $\ln S$ to the $\mathcal{O}(1)$ level, thereby partially softening (but not eliminating) the tension with SH0ES. Among the four ψ_i, no clear statistical preference emerges, though ψ_1 and ψ_4 tend to yield slightly higher concordance. Interestingly, there are two cases where the difference in suspiciousness is heavily marked: **SB + SN + H0** and **DB + SN + PI + H0**. For the former, ΛCDM presents markedly better concordance between data sets than the wavelets; for the latter, the converse holds. For **SB + SN + H0**, it can be argued that it is hard to reconcile the SDSS BAO data with PantheonPlus and SH0ES with wavelets, which is clear when we take into account that for this data set we have a poor performance in the data fit and the Bayesian evidence. Although this discordance is then alleviated if we include **PI** (thereby having **SB + SN + PI + H0**). We can again attribute this to a key feature of our wavelet constructions: they modify the late-time expansion history while leaving the comoving sound-horizon scale unchanged. The same argument can be made for **DB + SN + PI + H0**, where the wavelet naturally fits the DESI BAO while preserving the integrity of the background CMB data.

Let us investigate the results for a specific data set combination to see the effect that the SDSS-BAO likelihood has, and to show the similar behaviour of our wavelets of different orders. This case will be **SB + SN**, which presents a great fit of the data (the best out of all the **SB** cases) and relatively good Bayes' factors for every wavelet (all negative). The parameter $z^\dagger$ strongly favours values around $z = 2.3$. The specific values (with their 1σ uncertainties) are: 2.4 ± 1.0 for ψ_1, 2.44 ± 0.92 for ψ_2, 2.48 ± 0.96 for ψ_3, and 2.52 ± 0.98 for ψ_4. When examining the functional posteriors depicted in Fig. 5 concerning $H(z)/(1+z)$, the impact of the wavelets around $z \sim 2.4$ becomes evident. It can be deduced that the primary data set that influences the positioning of our wavelets is the high-redshift Lyman α BAO data given that it is localized at $z = 2.34$. This behaviour directly translates into the DE density as a possible transition from positive at low redshifts to negative at high redshifts, as seen in Fig. 5. This is particularly accentuated by the best-fits (red-dashed lines in Fig. 5) of wavelets ψ_2 and ψ_4, which have the lowest $-2\Delta\ln\mathcal{L}_{\max}$ overall (for the cases with **SB** in the data sets). This transition to a negative value is accentuated by the DE EoS parameter since it presents a pole ($\lim_{z\to z_p^\pm} w_{DE}(z) = \pm\infty$ with z_p being the point where DE density vanishes) when using the best-fitting values (dashed red lines in Fig. 5) close to $z = 2.5$. This pole, and asymptotic behaviour, has been observed in previous works considering effective DE densities changing sign (V. Sahni & Y. Shtanov 2003, 2005; S. Tsujikawa et al. 2008; S.-Y. Zhou, E. J. Copeland & P. M. Saffin 2009; F. Bauer, J. Sola & H. Stefancic 2010; V. Sahni, A. Shafieloo & A. A. Starobinsky 2014; A. Gomez-Valent, E. Karimkhani & J. Sola 2015; Y. Wang et al. 2018; O. Akarsu et al. 2020b, 2019, 2020a, 2021, 2023b, 2024a; E. Di Valentino et al. 2021a; G. Acquaviva et al. 2021; L. A. Escamilla & J. A. Vazquez 2023 E. Özülker 2022; R. Y. Wen et al. 2024; Ö. Akarsu et al. 2024d; Y. C. Ong 2023; S. Di Gennaro & Y. C. Ong 2022; Y. Tiwari et al. 2024; S. Dwivedi & M. Högås 2024; M. T. Manoharan 2024) and its presence is required when the DE density changes sign for a conserved DE (E. Özülker 2022). This feature of the DE density being able to attain negative values while also being able to oscillate makes the DE source derived from the wavelets a member of the omnipotent DE family (S. A. Adil et al. 2024).

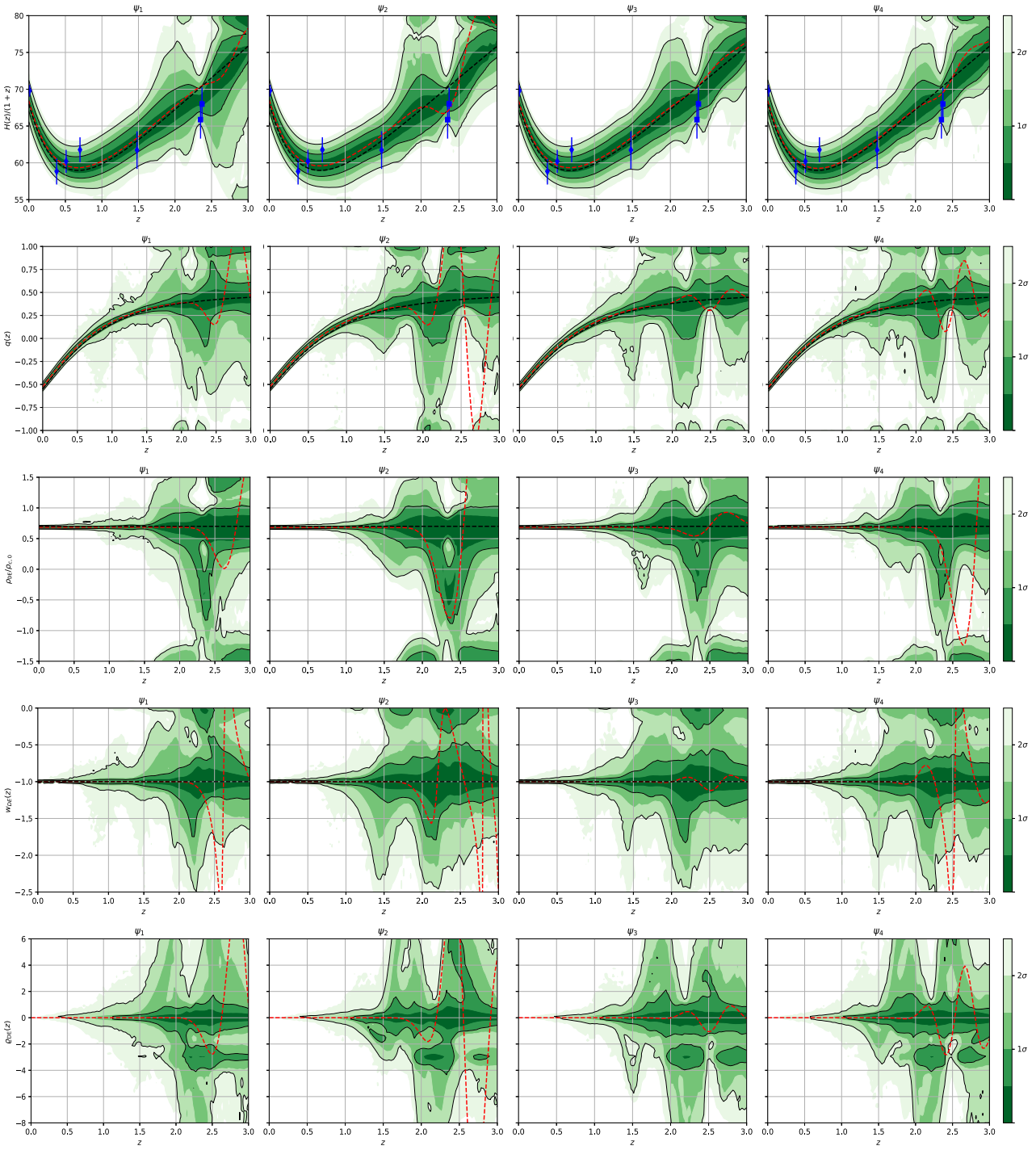

Figure 5. Functional posterior probability of $H(z)/(1+z)$, $q(z)$, $\rho_{\rm DE}(z)/\rho_{\rm c,0}$, $w_{\rm DE}(z)$, and $\varrho_{\rm DE}(z)$ for the data sets **SB + SN**. The probability, normalized in each slice of constant z, is shown with a color scale representing confidence interval values. The 68 per cent (1σ) and 95 per cent (2σ) confidence intervals are plotted as black lines. The dashed black line corresponds to the standard ΛCDM values, and the dashed red line represents the best-fitting values of the wavelets. These plots were made using the PYTHON library `fgivenx` (W. Handley 2018).

We continue the analysis of the functional posteriors depicted in Fig. 6, but this time for the data set **DB + SN** (to see how the change in BAO data affects the results). At first glance there is an obvious difference in the preferred position of the wavelet when compared to **SB**. Not only that but the overall magnitude of the oscillations is less. The wavelet is now localized in $z \sim 0.7$, and some of the characteristics described for **SB + SN** are absent, such as the asymptote in the DE EoS, or the clear preference for a switch to negative DE density.

However, even though Hermitian wavelets seem to be a good extension for the standard model, we cannot ignore how their influence translates into the deceleration parameter $q(z)$, which exhibits strong oscillatory behaviour, especially with ψ_2. This would imply significant changes in the dynamics of the Universe, directly

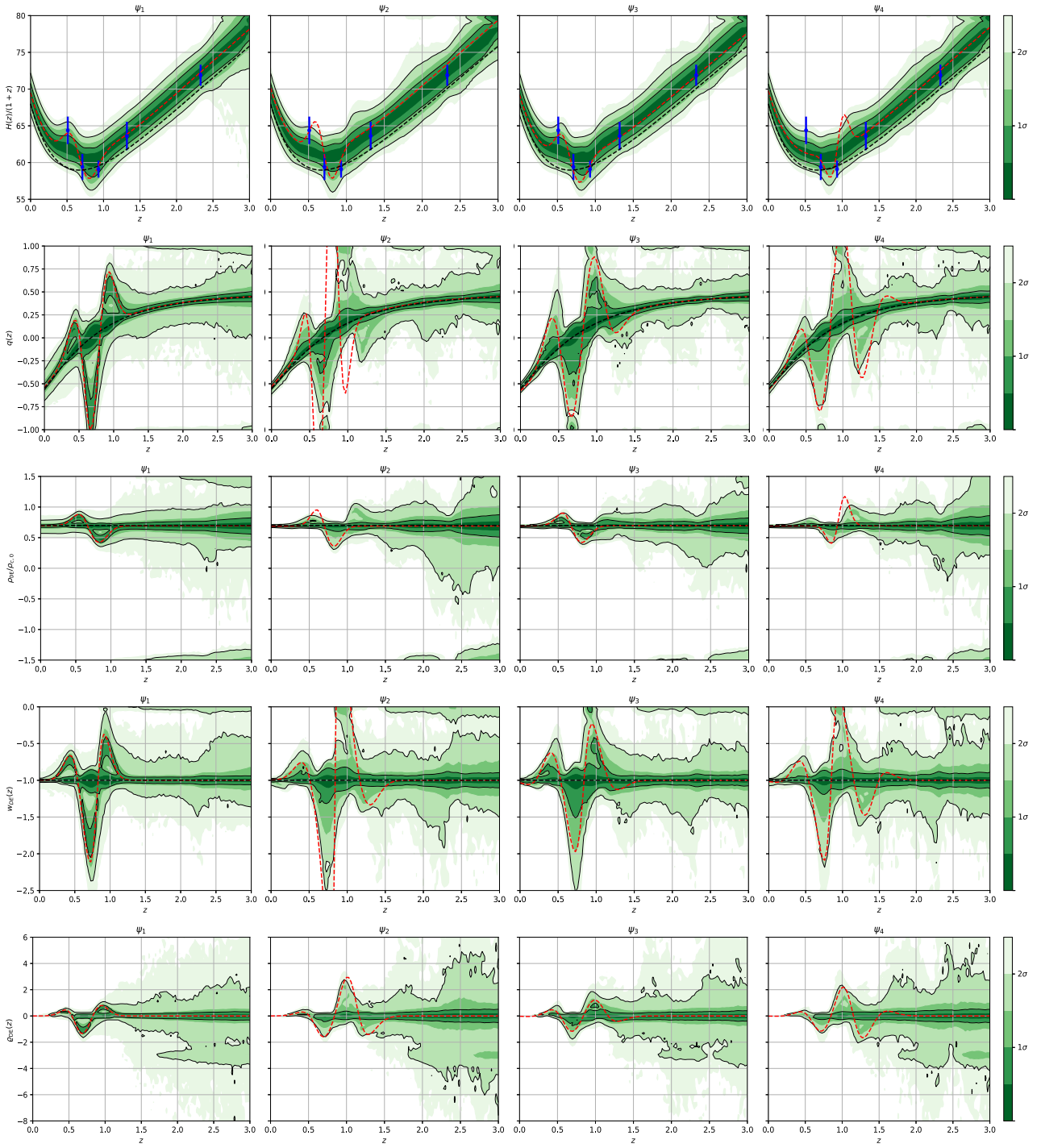

Figure 6. Functional posterior probability of $H(z)/(1+z)$, $q(z)$, $\rho_{\rm DE}(z)/\rho_{\rm c,0}$, $w_{\rm DE}(z)$, and $\varrho_{\rm DE}(z)$ for the data sets **DB + SN**. The probability, normalized in each slice of constant z, is shown with a color scale representing confidence interval values. The 68 per cent (1σ) and 95 per cent (2σ) confidence intervals are plotted as black lines. The dashed black line corresponds to the standard ΛCDM values, and the dashed red line represents the best-fitting values of the wavelets. These plots were made using the PYTHON library `fgivenx` (W. Handley 2018).

affecting structure formation (A. G. Riess et al. 1998; S. Perlmutter et al. 1999; Y. L. Bolotin et al. 2015; S. del Campo et al. 2012; D. M. Naik et al. 2023). These heavy oscillations are also evident in the DE density. The primary cause for this is the fact that the parameter β_h (which has a direct impact on the width and amplitude of the oscillations) is not constrained by the lack of data beyond $z = 2.34$. To fully resolve this issue, we would require data that cover a larger redshift region so that β_h can be fully characterized. Beyond $z = 2.5$, we can only speculate about the possible behaviour of the wavelets. Despite this issue, it is clear that **SB** prefers the Hermitian wavelet to exert its influence beyond $z \sim 1.5$, while **DB** is inclined towards $z \sim 0.7$.

Finally, we comment on the time derivative of the Hubble function as plotted in Fig. 7. When all the modifications to the Friedmann

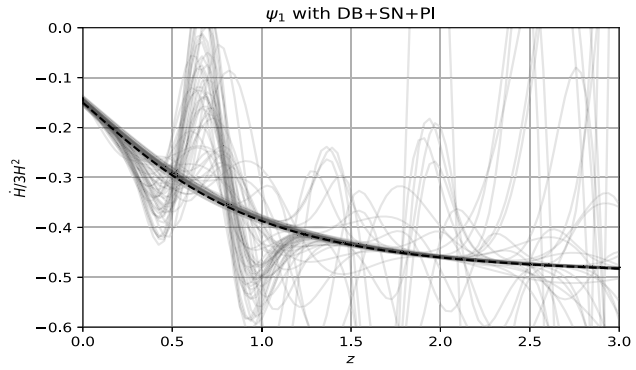

Figure 7. Functional posterior of the time derivative of the Hubble parameter, $\dot{H}$, normalized by the critical density, $3H^2$. The functional posterior was made with the reconstructed wavelet of first order, ψ_1, using the data set combination **DB + SN + PI**. The plot was made using the PYTHON library `fgivenx` (W. Handley 2018).

equations can be absorbed in the total energy density (ρ) and pressure (p) components of the energy–momentum tensor, this time derivative reads

$$\dot{H} = -\frac{1}{2}(\rho + p), \tag{18}$$

where the dot denotes differentiation with respect to cosmic time. Notice that the total inertial mass density $\varrho = \rho + p$ we discuss here is different from the DE inertial mass density, $\varrho_{\rm DE}$, shown in the last row of Fig. 5. Plotting equation (18) is of interest since if $\dot{H}$ is positive, the null energy condition is violated by the total energy–momentum content (which might include effective components originating from, say, a modified theory of gravity) of the Universe. The violation of the null energy condition and even the averaged null energy condition are abundant in physics; see the discussions and references in Refs. H. Epstein, V. Glaser & A. Jaffe 1965, R. M. Wald & U. Yurtsever 1991, M. Visser & C. Barcelo 2000, E. Curiel 2017, and E. Özülker 2022. As seen in the example case presented in Fig. 7 (corresponding to the case in Fig. 4 and the second panel of Fig. 3), some of the plotted lines from the posterior become positive at certain redshifts, indicating a violation of the null energy condition. However, this behaviour is not present in most of the samples and is not accentuated enough to make any claims regarding a preference for this behaviour from the available data. Moreover, we would expect the presence of this violation within the wavelet framework to be highly dependent on the type of wavelet that is chosen; e.g. a more squarely shaped wavelet would induce more abrupt oscillations in the Hubble parameter, causing this violation to be much more common in its constrained parameter space.

5 CONCLUSIONS

In this paper, we used a parameter inference procedure to analyse the behaviours of the Hubble function as preferred by background cosmological data. In this regard, we parametrized the Hubble function by considering deviations from the Hubble radius of ΛCDM in the form of wavelets as discussed in O. Akarsu et al. 2023b. Wavelets provide viable extensions of the ΛCDM model while preserving some features of it, such as the size of the comoving sound horizon and the fit to the measurement of its angular scale at last scattering.

All our reconstructions present a significant improvement in the fit to the data, reaching more than 3σ indication for wavelets when including DESI-BAO data. Most cases even present a negative Bayes' factor, indicating inconclusive or weak evidence in favour of wavelets (according to Jeffreys' scale), despite having three extra parameters. In line with the discussions in O. Akarsu et al. 2023b, a data set that exerts great influence on the behaviour of the wavelets is BAO, which can dictate where the wavelet will be localized. DESI-BAO prefers the centre of the wavelets to be at $z \sim 0.7$, while SDSS-BAO pushes it to $z \sim 2.3$. Our results indicate that this behaviour is driven by differences between the $D_H(z)/r_{\rm d}$ measurements of the two BAO data sets at $z < 1$ and $z \sim 2.3$, in particular, the discrepancy between the SDSS and DESI measurements at $z = 0.51$ and in their Lyman α BAO measurements. This discrepancy between the BAO data sets could be due to statistical fluctuations, but it is beyond the scope of this work to explore its cause. We also note that the improvement in the fit compared to ΛCDM is significantly larger for the DESI-BAO compared to SDSS, and the addition of our **SN** data set slightly ameliorates these improvements in line with the findings of the DESI collaboration for a preference of dynamical DE with BAO and SN Ia data (A. G. Adame et al. 2025).

We also showed how other derived quantities such as $q(z)$, $\rho_{\rm DE}$, and $w_{\rm DE}$ would behave and what effects the wavelets could have, particularly when SDSS-BAO is used. When the wavelet deviations are assumed to originate from a dynamical DE component, this DE presents some previously studied behaviours such as oscillations and a possible transition from a positive DE energy density to a negative one as redshift increases, making this DE a member of the omnipotent DE (S. A. Adil et al. 2024) family characterized by the combination of these two behaviours. While oscillations are present in $\rho_{\rm DE}$ by construction due to the oscillatory behaviours of the wavelets, the DE density attaining negative values in the past is a consequence of the data.

Despite the promising results obtained in this study, there is a problem involving the lack of data beyond a certain redshift value. For some cases involving the use of SDSS-BAO data, the centre of the wavelet, determined by the parameter $z^\dagger$, is located near $z \approx 2.4$, and our data only reach $z = 2.34$. Thus, there might be some features of the wavelets that simply cannot be constrained, such as the parameter $\beta_\hbar$. To address this, our only recourse is to await the availability of more data beyond this range, at which point we can revisit and re-perform the reconstructions done in this paper. It is also important to clarify that, despite presenting a better fit to the data, the Bayesian evidence in favour of the Hermitian wavelets is weak at best. The cause of this mainly being due to the three extra parameters.

We conclude by recognizing that Hermitian wavelets, on top of the Hubble radius of the standard ΛCDM model, in the late Universe show a lot of promise in capturing the dynamics of deviations from the standard model of cosmology at the background level without altering the early Universe and the constraints on the matter density and the Hubble constant. These behaviours can then be attributed to underlying physics, such as a dynamical dark energy component, and different underlying physics with the same background phenomena can be tested at the perturbative level with full data. It is worth noting that recent results from the DES collaboration, in particular the DES Y6 SN+BAO analysis (T. M. C. Abbott et al. 2025), report a deviation from ΛCDM at the 3.2σ level within the w_0w_aCDM parametrization, partly driven by the DES Y6 BAO measurement, which itself shows a $\sim 2\sigma$ tension with Planck ΛCDM. Furthermore, the recent DESI DR2 BAO release (M. Abdul Karim et al. 2025) provides significantly improved precision and also points towards indications of dynamical DE. Given the potential complementarity of these data sets, it will be important to assess their impact within our wavelet framework. We leave a detailed analysis including DES Y6

and DESI DR2 BAO for future work, where we expect the preference for dynamical features in the dark energy sector to become even more pronounced.

ACKNOWLEDGEMENTS

LAE was supported by CONAHCyT (Consejo Nacional de Humanidades, Ciencia y Tecnología) México. L.A.E. also acknowledges partial support from the Scientific and Technological Research Council of Türkiye (TÜBİTAK) under Grant No. 124N627. EÖ acknowledges support from the Türkiye Bilimsel ve Teknolojik Araştırma Kurumu (TÜBİTAK, Scientific and Technological Research Council of Turkey) through the 2214/A National Graduate Scholarship Program. ÖA acknowledges the support by the Turkish Academy of Sciences in scheme of the Outstanding Young Scientist Award (TÜBA-GEBİP). EDV is supported by a Royal Society Dorothy Hodgkin Research Fellowship. JAV acknowledges the support provided by FOSEC (Fondos Sectoriales) SEP-CONACYT Investigación Básica A1-S-21925,

UNAM-DGAPA-PAPIIT IN117723 and IN110325 (Universidad Nacional Autónoma de México, Dirección General de Asuntos del Personal Académico, Programa de Apoyo a Proyectos de Investigación e Innovación Tecnológica). We also want to thank the Unidad de Cómputo of ICF-UNAM (Instituto de Ciencias Físicas, UNAM) for their assistance in the maintenance and use of the computing equipment. This article is based upon work from COST Action CA21136 Addressing observational tensions in cosmology with systematics and fundamental physics (CosmoVerse) supported by COST (European Cooperation in Science and Technology).

DATA AVAILABILITY

The data underlying this article are available: the data sets encompass the SDSS Galaxy Consensus, quasars, and Lyman α forests in (F. Beutler et al. 2011; S. Alam et al. 2017, 2021; M. Ata et al. 2018; V. de Sainte Agathe et al. 2019; M. Blomqvist et al. 2019). The sound horizon is calibrated by using Big Bang Nucleosynthesis (E. Aubourg et al. 2015). The SN data set Pantheon + compilation are available in PantheonPlusSH0ES (2022). The CC data can be found within the public repository (M. Moresco 2015). The sampler code used in this work is available in A. Slosar & J. A. Vazquez (2019).

REFERENCES

Abazajian K. N. et al., 2009, ApJS, 182, 543
Abbott T. M. C. et al., 2022, Phys. Rev. D, 105, 023520
Abbott T. M. C. et al., 2023, Open J. Astrophys., 6, 2305.17173
Abbott T. M. C. et al., 2024, ApJ, 973, L14
Abbott T. M. C. et al., 2025, Dark Energy Survey: implications for cosmological expansion models from the final DES Baryon Acoustic Oscillation and Supernova data. preprint (arXiv:2503.06712)
Abdalla E. et al., 2022, JHEAp, 34, 49
Abdul Karim M. et al., 2025, Phys. Rev. D, 112, 40
Aboubrahim A., Nath P., 2024, JCAP, 09, 076
Acquaviva G., Akarsu O., Katirci N., Vazquez J. A., 2021, Phys. Rev. D, 104, 023505
Adam R. et al., 2016, A&A, 594, A1
Adame A. G. et al., 2025, JCAP, 02, 021
Adil S. A., Akarsu O., Malekjani M., Colgáin E. O., Pourojaghi S., Sen A. A., Sheikh-Jabbari M. M., 2023, MNRAS, 528, L20
Adil S. A., Akarsu O., Di Valentino E., Nunes R. C., Özülker E., Sen A. A., Specogna E., 2024, Phys. Rev. D, 109, 023527
Aghanim N. et al., 2020, A&A, 641, A6
Aiola S. et al., 2020, JCAP, 12, 047
Akarsu Ö., De Felice A., Di Valentino E., Kumar S., Nunes R. C., Özülker E., Vazquez J. A., Yadav A., 2024d, Phys. Rev. D, 110, 103527
Akarsu Ö., Perivolaropoulos L., Tsikoundoura A., Yükselci A. E., Zhuk A., 2025a, Dynamical dark energy with AdS-to-dS and dS-to-dS transitions: Implications for the H_0 tension. preprint (arXiv:2502.14667)
Akarsu Ö., Çam A., Paraskevas E. A., Perivolaropoulos L., 2025b, JCAP, 08, 089
Akarsu O., Barrow J. D., Board C. V. R., Uzun N. M., Vazquez J. A., 2019, Eur. Phys. J. C, 79, 846
Akarsu O., Katırcı N., Özdemir N., Vázquez J. A., 2020a, Eur. Phys. J. C, 80, 32
Akarsu O., Barrow J. D., Escamilla L. A., Vazquez J. A., 2020b, Phys. Rev. D, 101, 063528
Akarsu O., Kumar S., Özülker E., Vazquez J. A., 2021, Phys. Rev. D, 104, 123512
Akarsu O., Di Valentino E., Kumar S., Nunes R. C., Vazquez J. A., Yadav A., 2023a, Λ_sCDM model: A promising scenario for alleviation of cosmological tensions. preprint (arXiv:2307.10899)
Akarsu O., Colgain E. O., Özülker E., Thakur S., Yin L., 2023b, Phys. Rev. D, 107, 123526
Akarsu O., Kumar S., Özülker E., Vazquez J. A., Yadav A., 2023c, Phys. Rev. D, 108, 023513
Akarsu O., De Felice A., Di Valentino E., Kumar S., Nunes R. C., Ozulker E., Vazquez J. A., Yadav A., 2024a, Λ_sCDM cosmology from a type-II minimally modified gravity. preprint (arXiv:2402.07716)
Akarsu O., Bulduk B., De Felice A., Katırcı N., Uzun N. M., 2024, Phys. Rev. D, 112,, 083532
Akarsu O., Colgáin E. O., Sen A. A., Sheikh-Jabbari M. M., 2024c, Universe, 10, 305
Akarsu Ö., Colgáin E. Ó., Sen A. A., Sheikh-Jabbari M. M., 2025c, MNRAS, 542, L36
Alam U., Sahni V., Starobinsky A. A., 2004, JCAP, 06, 008
Alam S. et al., 2017, MNRAS, 470, 2617
Alam S. et al., 2021, Phys. Rev. D, 103, 083533
Alestas G., Camarena D., Di Valentino E., Kazantzidis L., Marra V., Nesseris S., Perivolaropoulos L., 2022, Phys. Rev. D, 105, 063538
Allali I. J., Aloni D., Schöneberg N., 2024, JCAP, 09, 019
Amanullah R. et al., 2010, ApJ, 716, 712
Anchordoqui L. A., Barger V., Marfatia D., Soriano J. F., 2022, Phys. Rev. D, 105, 103512
Anchordoqui L. A., Antoniadis I., Lust D., Noble N. T., Soriano J. F., 2024a, Phys. Dark Univ., 46, 101715
Anchordoqui L. A., Antoniadis I., Lust D., 2024b, Phys. Lett. B, 855, 138775
Ata M. et al., 2018, MNRAS, 473, 4773
Aubourg E. et al., 2015, Phys. Rev. D, 92, 123516
Bagherian H., Joseph M., Schmaltz M., Sivarajan E. N., 2025, Phys. Rev. D, 111, 043513
Balkenhol L. et al., 2023, Phys. Rev. D, 108, 023510
Baryakhtar M., Simon O., Weiner Z. J., 2024, Phys. Rev. D, 110, 083505
Bauer F., Sola J., Stefancic H., 2010, JCAP, 12, 029
Benisty D., Pan S., Staicova D., Di Valentino E., Nunes R. C., 2024, A&A, 688, A156
Bennett C. L. et al., 2013, ApJS, 208, 20
Bernardo R. C., Grandón D., Said Levi J., Cárdenas V. H., 2022, Phys. Dark Univ., 36, 101017
Bernui A., Di Valentino E., Giarè W., Kumar S., Nunes R. C., 2023, Phys. Rev. D, 107, 103531
Beutler F. et al., 2011, MNRAS, 416, 3017
Blomqvist M. et al., 2019, A&A, 629, A86
Bolotin Y. L., Cherkaskiy V. A., Lemets O. A., Yerokhin D. A., Zazunov L. G., 2015, Cosmology In Terms Of The Deceleration Parameter. Part I. preprint (arXiv:1502.00811)
Bonilla A., Kumar S., Nunes R. C., 2021, Eur. Phys. J. C, 81, 127
Bouhmadi-López M., Ibarra-Uriondo B., 2025, Phys. Rev. D, 112, 063559
Bousis D., Perivolaropoulos L., 2024, Phys. Rev. D, 110, 103546
Breuval L. et al., 2024, ApJ, 973, 30
Bull P. et al., 2016, Phys. Dark Univ., 12, 56

Calderón R., Gannouji R., L'Huillier B., Polarski D., 2021, Phys. Rev. D, 103, 023526
Calderon R. et al., 2024, JCAP, 10, 048
Castello S., Mancarella M., Grimm N., Sobral-Blanco D., Tutusaus I., Bonvin C., 2024, JCAP, 05, 003
Cervantes-Cota J. L., S. Galindo-Uribarri S., Smoot G. F., 2023, Universe, 9, 501
Chen S. et al., 2024, Phys. Rev. D, 110, 103518
Co R. T., Fernandez N., Ghalsasi A., Harigaya K., Shelton J., 2024, Phys. Rev. D, 110, 083534
Colgáin E. O., Sheikh-Jabbari M. M., Yin L., 2021, Phys. Rev. D, 104, 023510
Cruz J. S., Niedermann F., Sloth M. S., 2023, JCAP, 11, 033
Curiel E., 2017, Einstein Stud., 13, 43
Dalal R. et al., 2023, Phys. Rev. D, 108, 123519
de Sainte Agathe V. et al., 2019, ApJ, 878, 47
de Souza D. H. F., Rosenfeld R., 2023, Phys. Rev. D, 108, 083512
del Campo S., Duran I., Herrera R., Pavon D., 2012, Phys. Rev. D, 86, 083509
De Felice A., Mukohyama S., Pookkillath M. C., 2021, Phys. Lett. B, 816, 136201
Di Gennaro S., Ong Y. C., 2022, Universe, 8, 541
Di Valentino E., 2021, MNRAS, 502, 2065
Di Valentino E., 2022, Universe, 8, 399
Di Valentino E., Bridle S., 2018, Symmetry, 10, 585
Di Valentino E., Mena O., 2020, MNRAS, 500, L22
Di Valentino E., Melchiorri A., Silk J., 2016, Phys. Lett. B, 761, 242
Di Valentino E., Melchiorri A., Mena O., 2017, Phys. Rev. D, 96, 043503
Di Valentino E., Bøehm C., Hivon E., Bouchet F. R., 2018a, Phys. Rev. D, 97, 043513
Di Valentino E., Linder E. V., Melchiorri A., 2018b, Phys. Rev. D, 97, 043528
Di Valentino E., Ferreira R. Z., Visinelli L., Danielsson U., 2019, Phys. Dark Univ., 26, 100385
Di Valentino E., Melchiorri A., Mena O., Vagnozzi S., 2020, Phys. Dark Univ., 30, 100666
Di Valentino E., Mukherjee A., Sen A. A., 2021a, Entropy, 23, 404
Di Valentino E. et al., 2021b, Class. Quant. Grav., 38, 153001
Di Valentino E. et al., 2021c, Astropart. Phys., 131, 102604
Di Valentino E. et al., 2021d, Astropart. Phys., 131, 102605
Di Valentino E., Gariazzo S., Giunti C., Mena O., Pan S., Yang W., 2022, Phys. Rev. D, 105, 103511
Di Valentino E., Brout D., 2024, in The Hubble Constant Tension. Springer Series in Astrophysics and Cosmology, Springer
Di Valentino E. et al., 2025, Phys. Dark Univ., 49, 101965
Douspis M., Salvati L., Aghanim N., 2018, PoS, EDSU2018, 037
Dutta K., Ruchika Roy A., Sen A. A., Sheikh-Jabbari M. M., 2020, Gen. Rel. Grav., 52, 15
Dvornik A. et al., 2023, A&A, 675, A189
Dwivedi S., Högås M., 2024, Universe, 10, 406
Efron B., Gous A., Kass R. E., Datta G. S., Lahiri P., 2001, Lecture Notes-Monograph Series, 38, 208
Efstathiou G., Rosenberg E., Poulin V., 2024, Phys. Rev. Lett., 132, 221002
Epstein H., Glaser V., Jaffe A., 1965, Nuovo Cim., 36, 1016
Escamilla L. A., Vazquez J. A., 2023, Eur. Phys. J. C, 83, 251
Escamilla L. A., Akarsu O., Di Valentino E., Vazquez J. A., 2023, JCAP, 11, 051
Escamilla L. A., Akarsu Ö., Di Valentino E., Özülker E., Vazquez J. A., 2025, Exploring the Growth-Index (γ) Tension with Λ_sCDM. preprint (arXiv:2503.12945)
Faga L. et al., 2024, MNRAS, 536, 1586
Forconi M., Giarè W., Mena O., Ruchika Di Valentino E., Melchiorri A., Nunes R. C., 2024, JCAP, 05, 097
Frion E., Camarena D., Giani L., Miranda T., Bertacca D., Marra V., Piattella O. F., 2023, Open J. Astrophys., 7, 17
Garcia-Arroyo G., Ureña López L. A., Vázquez J. A., 2024, Phys. Rev. D, 110, 023529
Gariazzo S., Di Valentino E., Mena O., Nunes R. C., 2022, Phys. Rev. D, 106, 023530
Garny M., Niedermann F., Rubira H., Sloth M. S., 2024, Phys. Rev. D, 110, 023531
Giarè W., 2023, CMB Anomalies and the Hubble Tension. preprint (arXiv:2305.16919)
Giarè W., 2024, Phys. Rev. D, 109, 123545
Giarè W., Zhai Y., Pan S., Di Valentino E., Nunes R. C., van de Bruck C., 2024, Phys. Rev. D, 110, 063527
Giarè W., Betts J., van de Bruck C., Di Valentino E., 2025, Phys. Rev. Lett., 135, 071003
Gomez-Valent A., Solà Peracaula J., 2024, ApJ, 975, 64
Gómez-Valent A., Solà Peracaula J., 2025, Phys. Lett. B, 864, 139391
Gomez-Valent A., Karimkhani E., Sola J., 2015, JCAP, 12, 048
Gómez-Valent A., Favale A., Migliaccio M., Sen A. A., 2024, Phys. Rev. D, 109, 023525
Gómez-Vargas I., Esquivel R. M., García-Salcedo R., Vázquez J. A., 2023, Eur. Phys. J. C, 83, 304
Greene K. L., Cyr-Racine F.-Y., 2023, JCAP, 10, 065
Greene K., Cyr-Racine F.-Y., 2024, Phys. Rev. D, 110, 043524
Halder S., de Haro J., Saha T., Pan S., 2024, Phys. Rev. D, 109, 083522
Handley W., 2018, J. Open Source Softw., 3, 849
Handley W., Lemos P., 2019, Phys. Rev. D, 100, 043504
Harnois-Deraps J. et al., 2024, MNRAS, 534, 3305
Heisenberg L., Villarrubia-Rojo H., Zosso J., 2023, Phys. Dark Univ., 39, 101163
Heymans C. et al., 2021, A&A, 646, A140
Hoerning G. A., Landim R. G., Ponte L. O., Rolim R. P., Abdalla F. B., Abdalla E., 2025, Phys. Rev. D, 112, 023523
Högås M., Mörtsell E., 2023, Phys. Rev. D, 108, 124050
Högås M., Mörtsell E., 2025, Bimetric gravity improves the fit to DESI BAO and eases the Hubble tension. preprint (arXiv:2507.03743)
Jiang J.-Q., Pedrotti D., da Costa S. S., Vagnozzi S., 2024, Phys. Rev. D, 110, 123519
Jimenez R., Verde L., Treu T., Stern D., 2003, ApJ, 593, 622
Kamionkowski M., Riess A. G., 2023, Ann. Rev. Nucl. Part. Sci., 73, 153
Kass R. E., Raftery A. E., 1995, J. Am. Statist. Assoc., 90, 773
Kim J. et al., 2024, JCAP, 12, 022
Knox L., Millea M., 2020, Phys. Rev. D, 101, 043533
Kochappan J., Lu-Yin Lee B.-H., Ghosh T., 2024, Phys. Rev. D, 112, 9
Komatsu E. et al., 2011, ApJS, 192, 18
Krishnan C., Colgáin E. O., Ruchika Sen A. A., Sheikh-Jabbari M. M., Yang T., 2020, Phys. Rev. D, 102, 103525
Krolewski A., Percival W. J., Woodfinden A., 2025, Phys. Rev. Lett., 134, 101002
Kumar S., 2021, Phys. Dark Univ., 33, 100862
Kumar S., Nunes R. C., 2016, Phys. Rev. D, 94, 123511
Kumar S., Nunes R. C., 2017, Phys. Rev. D, 96, 103511
Lapi A., Boco L., Cueli M. M., Haridasu B. S., Ronconi T., Baccigalupi C., Danese L., 2023, ApJ, 959, 83
Lee N., Ali-Haïmoud Y., Schöneberg N., Poulin V., 2023, Phys. Rev. Lett., 130, 161003
Lee D. H., Yang W., Di Valentino E., Pan S., van de Bruck C., 2025, The Shape of Dark Energy: Constraining Its Evolution with a General Parametrization. preprint (arXiv:2507.11432)
Lewis A., 2025, JCAP, 08, 025
Li M., Li X.-D., Wang S., Wang Y., 2013, Front. Phys. (Beijing), 8, 828
Li S., Riess A. G., Casertano S., Anand G. S., Scolnic D. M., Yuan W., Breuval L., Huang C. D., 2024, ApJ, 966, 20
Liu G., Zhou Z., Mu Y., Xu L., 2023, Phys. Rev. D, 108, 083523
Lucca M., Hooper D. C., 2020, Phys. Rev. D, 102, 123502
Lynch G. P., Knox L., Chluba J., 2024, Phys. Rev. D, 110, 083538
Manoharan M. T., 2024, Eur. Phys. J. C, 84, 552
Mishra K. R., Pacif S. K. J., Kumar R., Bamba K., 2023, Phys. Dark Univ., 40, 101211
Montani G., Carlevaro N., Escamilla L. A., Di Valentino E., 2025, Phys. Dark Univ., 48, 101848
Moresco M., 2015, MNRAS, 450, L16
Moresco M., 2015, https://gitlab.com/mmoresco/CCcovariance

Moresco M., Verde L., Pozzetti L., Jimenez R., Cimatti A., 2012, JCAP, 07, 053
Moresco M. et al., 2016, JCAP, 05, 014
Mossa V. et al., 2020, Nature, 587, 210
Mukherjee P., Sen A. A., 2025, A New $\sim 5\sigma$ Tension at Characteristic Redshift from DESI-DR1 BAO and DES-SN5YR Observations. preprint (arXiv:2503.02880)
Murakami Y. S. et al., 2023, JCAP, 11, 046
Murgia R., Gariazzo S., Fornengo N., 2016, JCAP, 04, 014
Naik D. M., Kavya N. S., Sudharani L., Venkatesha V., 2023, Phys. Lett. B, 844, 138117
Niedermann F., Sloth M. S., 2021, Phys. Rev. D, 103, L041303
Niedermann F., Sloth M. S., 2022, Phys. Rev. D, 105, 063509
Niedermann F., Sloth M. S., 2023, New Early Dark Energy as a solution to the H_0 and S_8 tensions. preprint (arXiv:2307.03481)
Nunes R. C., Di Valentino E., 2021, Phys. Rev. D, 104, 063529
Nunes R. C., Pan S., Saridakis E. N., 2016, Phys. Rev. D, 94, 023508
Ong Y. C., 2023, Universe, 9, 437
Özülker E., 2022, Phys. Rev. D, 106, 063509
Özülker E., Di Valentino E., Giarè W., 2025, Dark Energy Crosses the Line: Quantifying and Testing the Evidence for Phantom Crossing. preprint (arXiv:2506.19053)
Padilla L. E., Tellez L. O., Escamilla L. A., Vazquez J. A., 2021, Universe, 7, 213
Pan S., Yang W., 2023, On the interacting dark energy scenarios – the case for Hubble constant tension. preprint (arXiv:2310.07260)
Pan S., Yang W., Di Valentino E., Shafieloo A., Chakraborty S., 2020, JCAP, 06, 062
Pan S., Seto O., Takahashi T., Toda Y., 2024, Phys. Rev. D, 110, 083524
PantheonPlusSH0ES, 2022, https://github.com/PantheonPlusSH0ES/DataRelease
Paraskevas E. A., Cam A., Perivolaropoulos L., Akarsu O., 2024, Phys. Rev. D, 109, 103522
Pedrotti D., Jiang J.-Q., Escamilla L. A., da Costa S. S., Vagnozzi S., 2025, Phys. Rev. D, 111, 023506
Percival W. J. et al., 2010, MNRAS, 401, 2148
Perivolaropoulos L., 2024, Phys. Rev. D, 110, 123518
Perivolaropoulos L., Skara F., 2022, New Astron. Rev., 95, 101659
Perlmutter S. et al., 1998, Nature, 391, 51
Perlmutter S. et al., 1999, ApJ, 517, 565
Pitrou C., Uzan J.-P., 2024, Phys. Rev. Lett., 132, 191001
Pogosian L. et al., 2022, Nat. Astron., 6, 1484
Poulin V., Boddy K. K., Bird S., Kamionkowski M., 2018, Phys. Rev. D, 97, 123504
Poulin V., Smith T. L., Karwal T., Kamionkowski M., 2019, Phys. Rev. Lett., 122, 221301
Poulin V., Smith T. L., Bartlett A., 2021, Phys. Rev. D, 104, 123550
Poulin V., Smith T. L., Karwal T., 2023, Phys. Dark Univ., 42, 101348
Poulin V., Smith T. L., Calderón R., Simon T., 2025, Phys. Rev. D, 111, 083552
Pourtsidou A., Tram T., 2016, Phys. Rev. D, 94, 043518
Raveri M., Pogosian L., Martinelli M., Koyama K., Silvestri A., Zhao G.-B., 2023, JCAP, 02, 061
Reid B. A. et al., 2010, MNRAS, 404, 60
Riess A. G. et al., 1998, Astron. J., 116, 1009
Riess A. G. et al., 2022, ApJ Lett., 934, L7
Rubin D. et al., 2023, ApJ, 986, 54
Ruchika P. L., Melchiorri A., 2025, Phys. Rev. D, 111, 123526
Ruchika Rathore H., Roy Choudhury S., Rentala V., 2024, JCAP, 06, 056
Sabogal M. A., Akarsu O., Bonilla A., Di Valentino E., Nunes R. C., 2024, Eur. Phys. J. C, 84, 703
Sabogal M. A., Silva E., Nunes R. C., Kumar S., Di Valentino E., 2025, Phys. Rev. D, 111, 043531
Sahni V., 2002, Class. Quant. Grav., 19, 3435
Sahni V., 2004, Lect. Notes Phys., 653, 141
Sahni V., Shtanov Y., 2003, JCAP, 11, 014
Sahni V., Shtanov Y., 2005, Phys. Rev. D, 71, 084018
Sahni V., Shafieloo A., Starobinsky A. A., 2014, ApJ Lett., 793, L40
Scherer M., Sabogal M. A., Nunes R. C., De Felice A., 2025, Phys. Rev. D, 112, 043513
Schöneberg N., Vacher L., 2025, JCAP, 03, 004
Schöneberg N., Franco Abellán G., Pérez Sánchez A., Witte S. J., Poulin V., Lesgourgues J., 2022, Phys. Rept., 984, 1
Scolnic D. M. et al., 2018, ApJ, 859, 101
Sen A. A., Adil S. A., Sen S., 2022, MNRAS, 518, 1098
Seto O., Toda Y., 2024, Phys. Rev. D, 110, 083501
Silva E., Zúñiga-Bolaño U., Nunes R. C., Di Valentino E., 2024, Eur. Phys. J. C, 84, 1104
Silva E., Sabogal M. A., Scherer M., Nunes R. C., Di Valentino E., Kumar S., 2025, Phys. Rev. D, 111, 123511
Simon J., Verde L., Jimenez R., 2005, Phys. Rev. D, 71, 123001
Slosar A., Vazquez J. A., 2019, 00. https://github.com/ja-vazquez/SimpleMC
Smith T. L., Poulin V., Amin M. A., 2020, Phys. Rev. D, 101, 063523
Soriano J. F., Wohlberg S., Anchordoqui L. A., 2025, Phys. Dark Univ., 48, 101911
Souza M. S., Barcelos A. M., Nunes R. C., Akarsu Ö., Kumar S., 2025, Universe, 11, 2
Speagle J. S., 2020, MNRAS, 493, 3132
Specogna E., Adil S. A., Ozulker E., Di Valentino E., Nunes R. C., Akarsu O., Sen A. A., 2025, Updated Constraints on Omnipotent Dark Energy: A Comprehensive Analysis with CMB and BAO Data. preprint (arXiv:2504.17859)
Stern D., Jimenez R., Verde L., Kamionkowski M., Stanford S. A., 2010, JCAP, 02, 008
Tamayo D., Vazquez J. A., 2019, MNRAS, 487, 729
Tang X., Ma Y.-Z., Dai W.-M., He H.-J., 2024, Phys. Dark Univ., 46, 101568
Tiwari Y., Ghosh B., Jain R. K., 2024, Eur. Phys. J. C, 84, 220
Toda Y., Giarè W., Özülker E., Di Valentino E., Vagnozzi S., 2024, Phys. Dark Univ., 46, 101676
Tröster T. et al., 2020, A&A, 633, L10
Trotta R., 2008, Contemp. Phys., 49, 71
Tsujikawa S., Uddin K., Mizuno S., Tavakol R., Yokoyama J., 2008, Phys. Rev. D, 77, 103009
Vagnozzi S., 2023, Universe, 9, 393
van der Westhuizen M. A., Abebe A., 2024, JCAP, 01, 048
Vazquez J. A., Bridges M., Hobson M. P., Lasenby A. N., 2012, JCAP, 09, 020
Verde L., Treu T., Riess A. G., 2019, Nat. Astron., 3, 891
Verde L., Schöneberg N., Gil-Marín H., 2024, Ann. Rev. A&A, 62, 287
Visinelli L., Vagnozzi S., Danielsson U., 2019, Symmetry, 11, 1035
Visser M., Barcelo C., 2000, in 3rd International Conference on Particle Physics and the Early Universe. p. 98 , preprint (arXiv:gr-qc/0001099)
von Marttens R., Lombriser L., Kunz M., Marra V., Casarini L., Alcaniz J., 2020, Phys. Dark Univ., 28, 100490
Wald R. M., Yurtsever U., 1991, Phys. Rev. D, 44, 403
Wang Y., Pogosian L., Zhao G.-B., Zucca A., 2018, ApJ Lett., 869, L8
Wang L.-M., Caldwell R. R., Ostriker J. P., Steinhardt P. J., 2000, ApJ, 530, 17
Weinberg S., 1989, Rev. Mod. Phys., 61, 1
Weinberg D. H., Mortonson M. J., Eisenstein D. J., Hirata C., Riess A. G., Rozo E., 2013, Phys. Rept., 530, 87
Wen R. Y., Hergt L. T., Afshordi N., Scott D., 2024, JCAP, 03, 045
Yadav A., Kumar S., Kibris C., Akarsu O., 2025, JCAP, 01, 042
Yang W., Mukherjee A., Di Valentino E., Pan S., 2018, Phys. Rev. D, 98, 123527
Yang W., Di Valentino E., Mena O., Pan S., Nunes R. C., 2020a, Phys. Rev. D, 101, 083509
Yang W., Di Valentino E., Pan S., Basilakos S., Paliathanasis A., 2020b, Phys. Rev. D, 102, 063503
Yang W., Di Valentino E., Pan S., Shafieloo A., Li X., 2021a, Phys. Rev. D, 104, 063521
Yang W., Di Valentino E., Pan S., Wu Y., Lu J., 2021b, MNRAS, 501, 5845
Yao Y.-H., Meng X.-H., 2023, Phys. Dark Univ., 39, 101165
Ye G., Piao Y.-S., 2020, Phys. Rev. D, 101, 083507
Ye G., Zhang J., Piao Y.-S., 2023, Phys. Lett. B, 839, 137770

Zhai Y., Giarè W., van de Bruck C., Di Valentino E., Mena O., Nunes R. C., 2023, JCAP, 07, 032
Zhang C., Zhang H., Yuan S., Zhang T.-J., Sun Y.-C., 2014, Res. A&A, 14, 1221
Zhou S.-Y., Copeland E. J., Saffin P. M., 2009, JCAP, 07, 009

APPENDIX A: ADDITIONAL CONSTRAINTS AND FIGURES

For completeness, we provide some results for the other reconstructed wavelets, although this might seem redundant given how similar they are. It is no surprise that most of the outcomes and behaviours reconstructed for ψ_1 are shared by the rest of the Hermitian wavelets, given their similarities. This is easily verifiable by comparing Fig. 2 with Fig. A1 and Fig. 3 with Fig. A5. Despite using different Hermitian wavelets, the constraints on the parameter $z^\dagger$ remain essentially the same, and the Hubble functions show only minor variations, primarily driven by the choice of data sets. Therefore, we have opted not to extend the discussion to the other wavelets.

A topic that requires some discussion is the result of the parameter inference procedure on the other two wavelet parameters, α_h and β_h, found in Figs A2 and A3, respectively. For α_h, we observe a similar behaviour to that displayed by $z^\dagger$, in the sense that the BAO data set is the primary driver of parameter inference, not **SN** or **Pl**. We also observe bimodality in some cases and a lack of convergence in others. The parameter β_h, on the other hand, has very little impact on the data sets used. In Fig. A3, it is evident that β_h remains largely unconstrained in most cases within the prior range considered. Several exceptions exist, where a faint maximum appears, such as in ψ_2 or ψ_4 with **SB + SN**. This lack of a well-defined posterior is expected for this particular parameter, given its minimal impact on the overall wavelet behaviour (as shown in Fig. 1) and the limited data available beyond $z \sim 2.3$, as discussed in Section 4. Although these parameters do play a role in the shape of the wavelet, their overall impact is less significant than that of $z^\dagger$. Therefore, their discussion has been reserved for this appendix.

Finally, and to aid in the understanding and clarity of the results presented in this study with regard to the reconstructed $H(z)/(1+z)$, we include additional figures that provide enhanced visualizations of the wavelet behaviour in the late Universe. These figures are artistically adapted versions of the previously shown plots in Fig. 3, designed to improve readability and facilitate a clearer interpretation of the data.

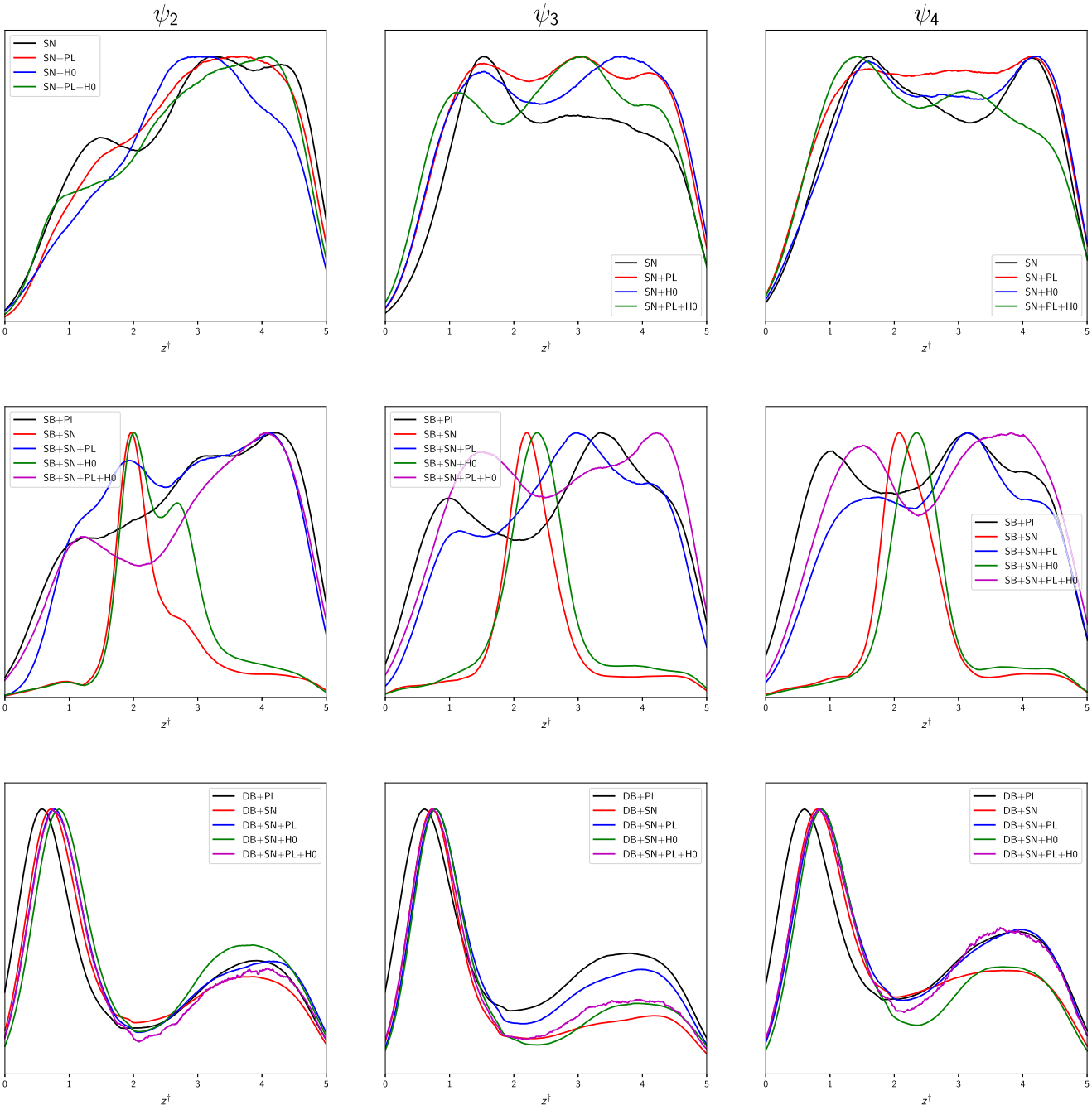

Figure A1. 1D marginalized posterior distributions for the reconstructed parameter $z^\dagger$ for (from left to right) $\psi_2(z)$, $\psi_3(z)$, and $\psi_4(z)$. We present the results in three different panels to illustrate the effect of the BAO data sets on the posteriors. These plots were created using the PYTHON library GETDIST (A. Lewis 2025).

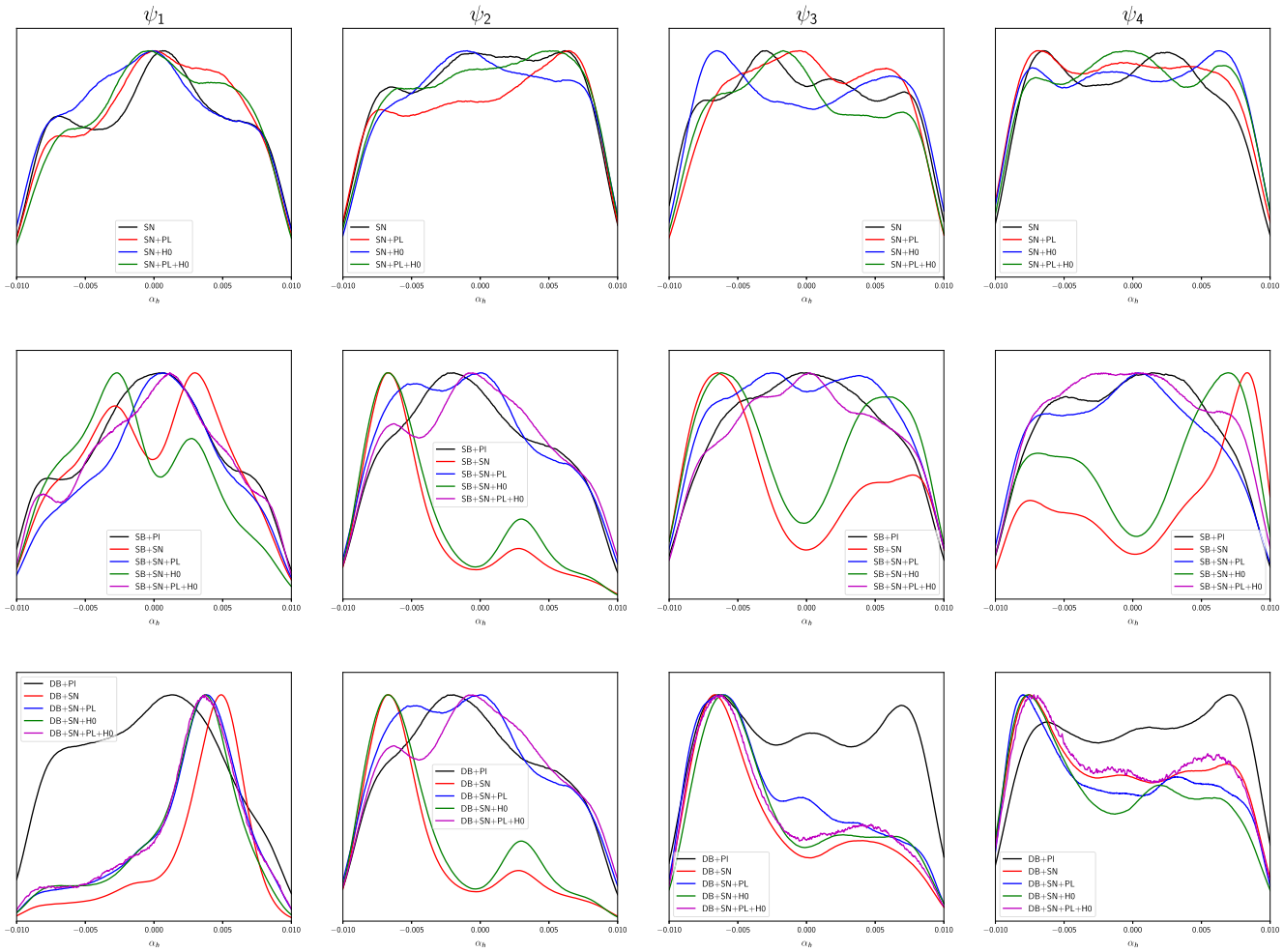

Figure A2. 1D marginalized posterior distributions for the reconstructed parameter α_h for, from left to right, $\psi_2(z)$, $\psi_3(z)$, and $\psi_4(z)$. We present the results in three different panels to illustrate the effect of the BAO data sets on the posteriors. These plots were created using the PYTHON library GETDIST (A. Lewis 2025).

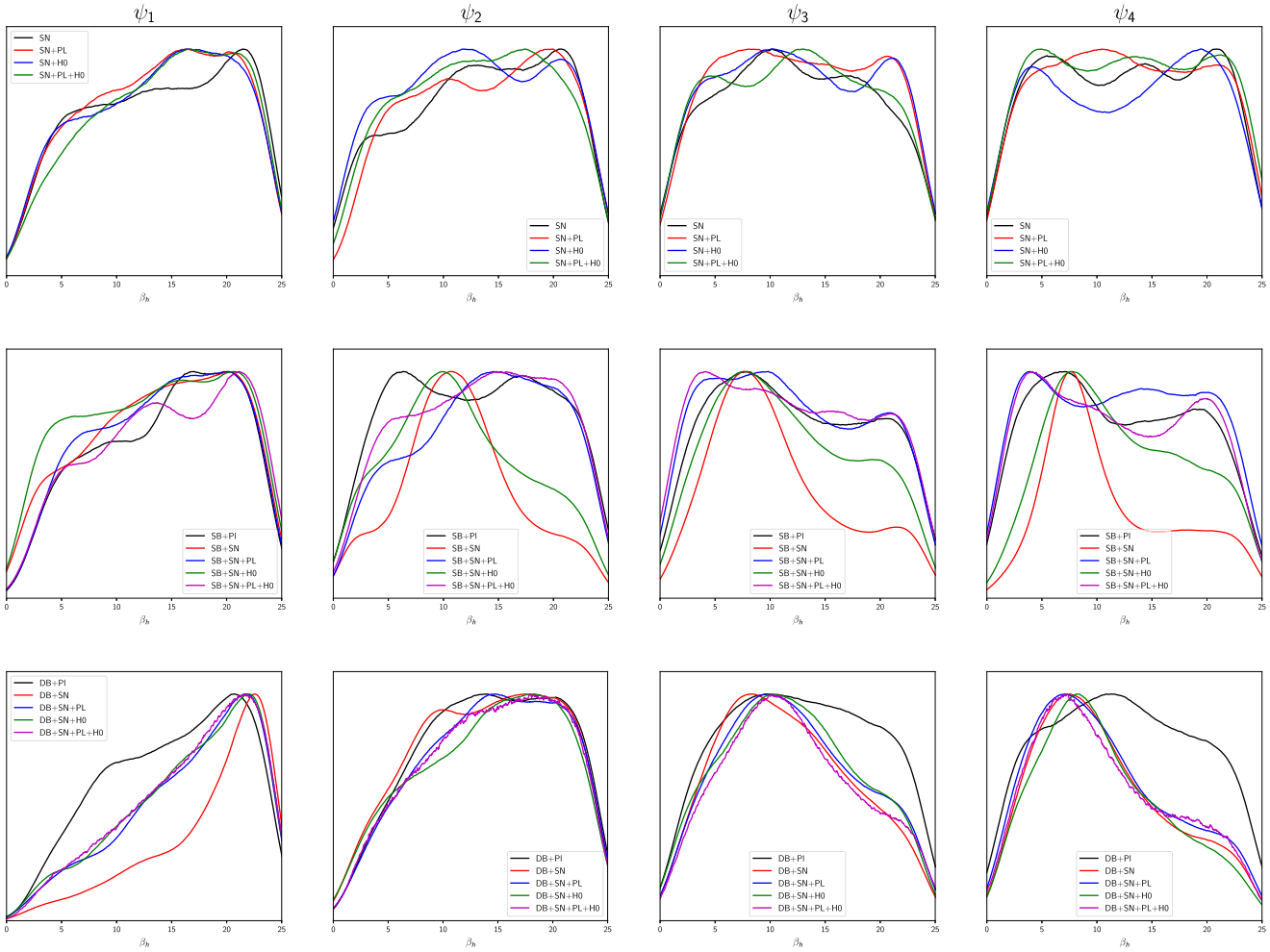

Figure A3. 1D marginalized posterior distributions for the reconstructed parameter β_h for, from left to right, $\psi_1(z)$, $\psi_2(z)$, $\psi_3(z)$, and $\psi_4(z)$. We present the results in three different panels to illustrate the effect of the BAO data sets on the posteriors. These plots were created using the PYTHON library GETDIST (A. Lewis 2025).

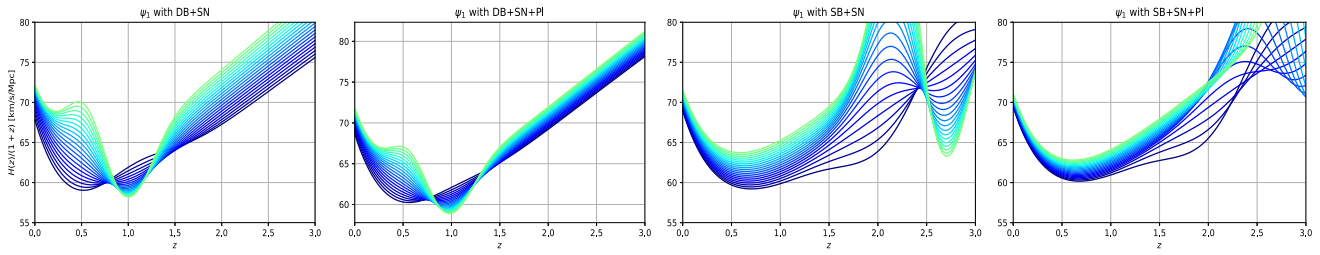

Figure A4. Artistically adapted version of Fig. 3 to enhance the readability of wavelet behaviour in the late Universe.

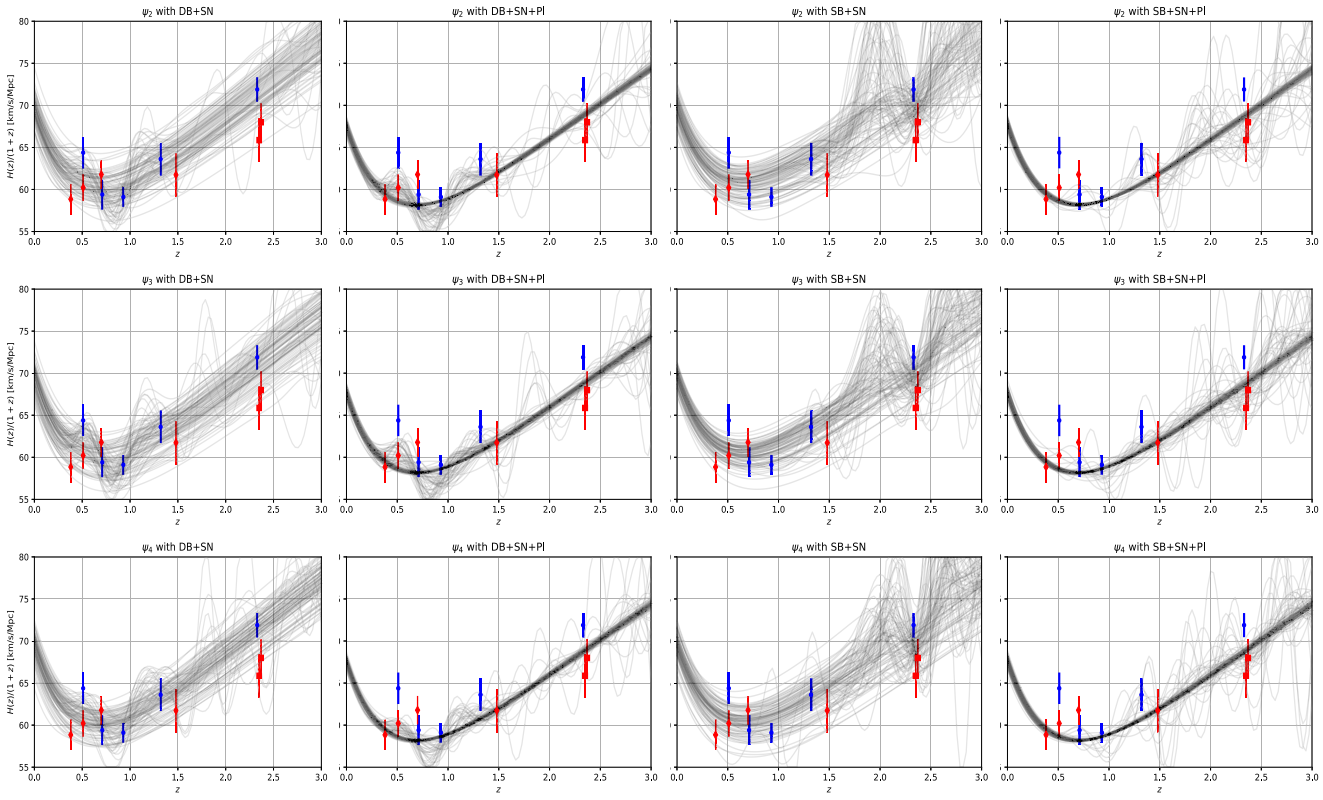

Figure A5. Functional posterior for $H(z)/(1+z)$ for $\psi_1(z)$ using four distinct data combinations: **DB + SN**, **DB + SN + Pl**, **SB + SN**, and **SB + SN + Pl**. The red (blue) error bars correspond to the SDSS (DESI) BAO distance $D_H(z)/r_{\rm d}$ measurements. The size of the sound horizon was fixed at the robust value of 147 Mpc to highlight the BAO data in the figure. The plots were created using the PYTHON library `fgivenx` (W. Handley 2018).

This paper has been typeset from a TEX/LATEX file prepared by the author.